

Here is a sample chapter from this book.

This sample chapter is copyrighted and made available for personal use only. No part of this chapter may be reproduced or distributed in any form or by any means without the prior written permission of Medical Physics Publishing.

In-line Phase-sensitive X-ray Imaging

Da Zhang¹, Fanbo Meng², John Rong³, Xizeng Wu⁴, and Hong Liu^{5}*

¹ Massachusetts General Hospital

²GE Healthcare China

³University of Texas MD Anderson Cancer Center

⁴University of Alabama at Birmingham

⁵University of Oklahoma

**Corresponding Author*

10.1	Introduction	144
10.1.1	Phase-contrast vs. Attenuation-based X-ray Imaging	144
10.1.2	In-line and Other Phase-sensitive X-ray Imaging Techniques.....	144
10.2	Physics Principles of In-line X-ray Phase-contrast Imaging	145
10.2.1	Attenuation, Phase Shift, and Optical Transmission	145
10.2.2	System Configuration of In-line Phase-contrast Imaging.....	145
10.2.3	Theoretical Framework of In-line Phase-contrast Imaging with Ideal Imaging Systems	145
10.2.4	Partial Spatial Coherence and Optical Transfer Functions.....	147
10.2.5	A Full Phase-space Theoretical Framework.....	148
10.2.6	Phase-contrast Imaging vs. Phase Retrieval	150
10.3	Design Considerations and Clinical Implementation of In-line X-ray Phase-sensitive Imaging	151
10.3.1	Coherence Requirement in the Clinical Implementation of Phase Contrast Imaging	151
10.3.2	Analysis Based Upon Relative Phase Factor (RPF)	152
10.4	Progress in System Development and Current Status of In-line Phase-contrast Imaging	157
10.4.1	The Design, Development, and Performance Characterization of a Dual Detector In-line Phase-contrast Imaging System.....	157
10.4.2	Preclinical Experiments and Subjective Evaluations.....	160
10.4.3	Phase Duality-based Robust Phase Retrieval	165
10.5	Summary	168
10.6	Acknowledgment	168
10.7	References.....	168

10.1 Introduction

10.1.1 Phase-contrast vs. Attenuation-based X-ray Imaging

In x-ray diagnostic imaging, it is very important to obtain good tissue contrast and noise characteristics while keeping radiation dose as low as achievable. There are three well-known effects that lead to the attenuation for photon energies up to 1 MeV (i.e., below the threshold for the pair production): coherent scattering, which is elastic with no energy loss; incoherent scattering, which is inelastic with energy transferred to tissue; and photoelectric interactions, where energy is given to free a bound electron. These processes form the basis for our understanding of traditional attenuation-based x-ray imaging.

In addition to attenuation, however, tissue contrast can also be realized from the x-ray phase change generated by tissues. While attenuation-based tissue contrast has been the primary mechanism for generating medical images for the past century, the utility of phase-based tissue contrast has only recently been recognized (Wilkins et al. 1996). X-ray phase change arises from no new x-ray–tissue interaction; rather it is a result of coherent x-ray scattering, relying upon the wave properties of light. Like any wave field, a coherent x-ray wave field propagating along the z-axis can be described as

$$\psi(x, z) = \sqrt{I(x)} \exp(ikz) \quad (10.1)$$

where x is the coordinate for the transverse direction, $k = 2\pi/\lambda$, λ is the x-ray wavelength, and $I(x)$ is the x-ray intensity. In this case, the phase of the x-ray wave is kz . When an x-ray scatters from tissue, the phase of the x-ray wave field is altered. This phase change is the result of coherent scattering with small angles, and it includes both diffraction and refraction effects. The magnitude of the phase change is determined by the biological tissue dielectric susceptibility, or equivalently, by the refractive index of the tissue. The refractive index n for an x-ray is complex and equals to

$$n = 1 - \delta - i\beta \quad (10.2)$$

where δ , the refractive index decrement, is responsible for the x-ray phase shift, and β is responsible for x-ray absorption. δ is given by (Wilkins et al. 1996):

$$\delta = \left(\frac{r_e \lambda^2}{2\pi}\right) \sum_k N_k (Z_k + f_k^r) \quad (10.3)$$

where r_e , N_k , Z_k , and f_k^r are the classical electron radius, atomic density, atomic number, and real part of the anomalous atomic scattering factor of the element k , respectively. If the

x-ray energy is away from the absorption edge of tissue, the above formula can be simplified to

$$\begin{aligned} \delta &= \left(\frac{r_e \lambda^2}{2\pi}\right) \sum_k N_k (Z_k + f_k^r) \\ &\cong \left(\frac{r_e \lambda^2}{2\pi}\right) \rho_e = (4.49 \times 10^{-16}) \lambda^2 \rho_e \end{aligned} \quad (10.4)$$

where $\rho_e = \sum_k N_k Z_k$ is the electron density. Though x-ray absorption is obvious in many radiological medicine procedures, x-ray refraction by human tissue usually goes unnoticed. This is not because the tissue δ is too small compared to β . On the contrary, tissue δ values (10^{-6} to 10^{-8}) are on the order of 1000 times greater than β (10^{-9} to 10^{-11}) for x-rays in the 10 keV to 100 keV range. Thus, it is not without irony that all previous x-ray clinical imaging techniques until recently were designed to image tissue's β but not δ . Using the formula for refractive index decrement δ , the amount of x-ray phase change imparted by biological tissue can be calculated as

$$\phi = -\frac{2\pi}{\lambda} \int \delta(s) ds \quad (10.5)$$

where s is the distance traveled by the x-ray beam along the vacuum propagation direction.

10.1.2 In-line and Other Phase-sensitive X-ray Imaging Techniques

At this stage of development there are four major different modes for phase imaging: crystal analyzer-based x-ray interferometry, grating-based differential phase-contrast imaging, diffraction-enhanced imaging, and in-line phase-contrast imaging. X-ray interferometry images the phase ϕ itself directly using monochromatic x-rays from synchrotron radiation and a monochromator crystal (Momose and Fukuda 1995). Grating-based differential phase-contrast imaging employs phase and absorption gratings as a lateral shearing interferometer to measure the subject's phase gradient $\nabla\phi$ directly (Momose 2003; Weitkamp et al. 2005). Diffraction-enhanced imaging (Chapman et al. 1997) measures the phase gradient $\nabla\phi$ directly, also using monochromatic x-rays from synchrotron radiation. In-line phase-contrast imaging measures the Laplacian of phase $\nabla^2\phi$ directly (Wilkins et al. 1996). This mode can be implemented with polychromatic x-rays from an x-ray tube. Since x-ray tubes are compact and relatively readily available, this mode has potential for clinical applications, and is the topic of this chapter.

10.2 Physics Principles of In-line Phase-contrast Imaging

10.2.1 Attenuation, Phase Shift, and Optical Transmission

The setting of in-line phase-contrast imaging is similar to conventional radiography, but the object-to-detector distance is larger. Consider a plane wave x-ray source. If the x-ray projection is along the z-axis direction, we can then model the phase shift and attenuation effects of a body part as a two-dimensional transmission function $T(x, y)$ in the x-y plane

$$T(x, y) = A(x, y)e^{i\phi(x, y)}, \quad (10.6)$$

where $\phi(x, y)$ is determined by the z-projection of the object's δ :

$$\phi(x, y) = \frac{-2\pi}{\lambda} \int \delta(x, y, z) dz = -\lambda r_e \rho_{e,p}(x, y), \quad (10.7)$$

where $\rho_{e,p}(x, y) = \int \rho_e(x, y, z) dz$ is the projected electron density, and $A(x, y)$ is determined by the z-projection of the object's β

$$A(x, y) = \exp\left(-\frac{2\pi}{\lambda} \int \beta(x, y, z) dz\right). \quad (10.8)$$

$T(x, y)$ connects the incident and the transmitted wave field by $E(x, y) = E_{in}(x, y) \times T(x, y)$. It is independent of the incident wave, and is a measure of the internal structure of the tissue in terms of the induced attenuation and phase shift, which are accounted for by $A(x, y)$ and $\phi(x, y)$, respectively. In other words, $A(x, y)$ and $\phi(x, y)$ carry different information about the internal structure of the tissue.

In order to accurately model an object by Equation 10.6, the object must be thin enough that the projection approximation holds, i.e., the x-ray transmits the object along a straight line. If t is the object's thickness, it can be shown that as long as the size of the finest feature to be imaged is larger than $\sqrt{\lambda t}$, the object can be deemed thin (Wu et al. 2003). It has

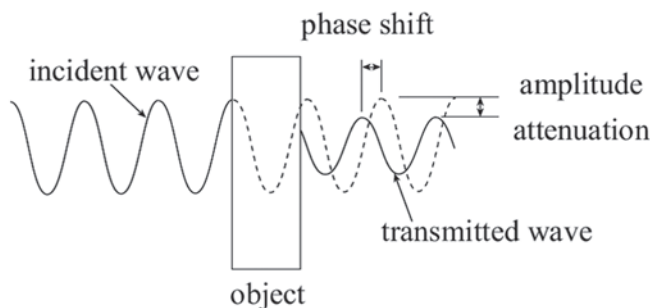


Figure 10–1. Schematic showing the amplitude attenuation and phase shift of x-ray wave by an object.

been proven that human body parts can be treated as thin objects for resolutions as high as 10 microns for x-ray photon energies ranging from 10 keV to 150 keV (Wu et al. 2003). Therefore, it is appropriate to model the human body using Equation 10.6 for diagnostic x-ray imaging.

Figure 10–1 shows schematically the amplitude attenuation and phase shift induced by an object when an x-ray wave passes through it. Figure 10–2 illustrates the image formation of in-line phase contrast x-ray imaging.

10.2.3 System Configuration of In-line Phase Contrast Imaging

In-line phase-contrast imaging techniques unveil the effects of phase shifts based on x-ray wave propagation, and can be implemented with relatively simple imaging system configuration, without the need for precise optical devices such as collimators and monochromators. This particular feature makes it possible to readily implement such a system in clinics and hospitals.

Figure 10–3 shows the schematic of a typical system configuration. The x-ray radiation from the point x-ray source penetrates the sample object and reaches the image detector. We denote the source to object distance (SOD) as R_1 and the object to image distance (OID) as R_2 ; thus, the source to image distance (SID) is $R_1 + R_2$. This forms a magnification configuration, where the image magnification M can then be written as $M = (R_1 + R_2)/R_1$.

In this chapter, an image taken with $M=1$ ($R_2=0$) is called an “attenuation-based” image I_{ab} , since it contains only information about the object's attenuation. The detector is placed closely behind the object and no phase effects are recorded in the image. A “phase-contrast” image I_{pc} , on the other hand, is taken with $M > 1$ ($R_2 > 0$). With a propagation distance R_2 , the x-ray manifests the phase shift in wave-front curvature and, hence, intensity change as determined by diffraction principles. Image contrasts come from both attenuation and phase shifts, and thus what the I_{pc} records is a “phase-enhanced” image.

10.2.3 Theoretical Framework of In-line Phase Contrast Imaging with Ideal Imaging Systems

In order to describe the theories underlying in-line phase contrast imaging, we will first present a general theoretical for-

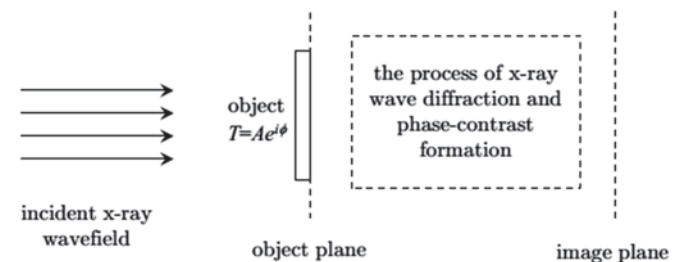


Figure 10–2. The image formation in phase contrast x-ray imaging.

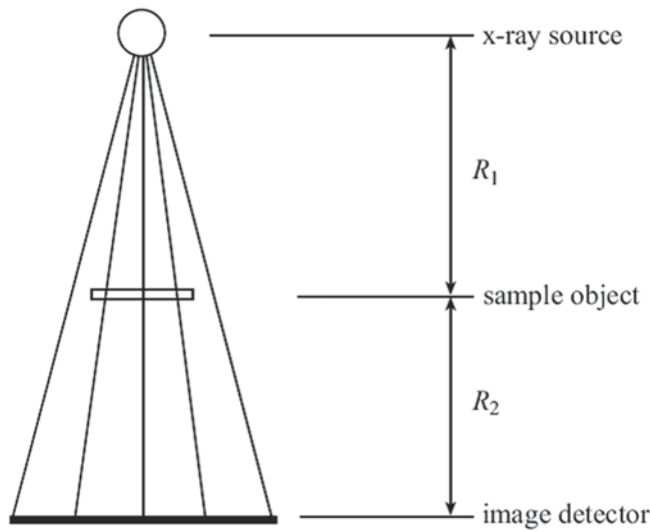


Figure 10–3. The system configuration of in-line phase contrast imaging and quantitative phase imaging.

mulation for ideal imaging systems, and then extend it to systems with non-ideal x-ray sources and detectors and present a full phase-space theoretical framework based upon the Wigner distribution.

In-line phase-contrast imaging is based on Fresnel diffraction of x-rays. Our strategy is to model the Fresnel diffraction process and relate the object transmission function to image intensity. Let us first analyze an imaging system in which the x-ray source is a monochromatic and, ideally, small point source, and the detectors are of unlimited resolution. The point source of wavelength λ is located at $x_0 = 0, y_0 = 0$. The distance from the source to the object, R_1 , and from the object plane to the detector plane, R_2 , are shown in Figure 10–3.

Applying the paraxial Fresnel diffraction theory to the point source geometry, one can write the diffracted spherical x-ray wave field arriving at a location (x, y) on the detector plane as a Fresnel–Kirchhoff integral (Born and Wolf 1980):

$$E(x, y) = \frac{\sqrt{R_1 I_0}}{\sqrt{i\lambda R_2 (R_1 + R_2)}} \exp\left(i\pi \frac{2(R_1 + R_2)^2 + y^2}{\lambda(R_1 + R_2)}\right) \int_{-\infty}^{\infty} \exp\left[i\frac{\pi}{\lambda} \left(\frac{\eta^2}{R_1} + \frac{(\eta - x)^2}{R_2}\right)\right] T(\eta) d\eta \quad (10.9)$$

In Equation 10.9, integrating over the variable η convolves $T(x)$ with the Fresnel-diffraction propagator. For easy comparisons but without loss of generality, we assume that the object transmission T does not depend on y , but later we

will generalize the results to the 2D case. I_0 is the incident x-ray intensity at R_1 .

Instead of calculating the Fourier transform (FT) of the wave amplitude as done in a previous work (Pogany et al. 1997), our theory was based on the direct FT of the x-ray diffraction intensity (Wu and Liu 2003a). In order to achieve this, we derived the x-ray intensity image $I(x)$ at the detector plane, in a symmetric form:

$$I(x) = |E(x, y)|^2 = \frac{I_0}{\lambda M R_2} \int_{-\infty}^{\infty} \int_{-\infty}^{\infty} \exp\left(i\pi M \frac{(\eta_1 - x/M)^2 - (\eta_2 - x/M)^2}{\lambda R_2}\right) T(\eta_1) T^*(\eta_2) d\eta_1 d\eta_2, \quad (10.10)$$

where $I_0 = E_0^2$ is the incident intensity at the object plane, T^* is the complex conjugate of the transmission function, and M is the magnification, defined previously.

The x-ray image intensity distribution at the detector plane $I(x)$ in the above equation is a complicated function of the object’s attenuation and phase. As the integral is difficult to carry out analytically, we attempt to conduct a spatial frequency analysis of $I(x)$ to see how the spatial frequency information of object attenuation and phase are transferred to the detector plane.

Considering the Fourier transform (FT) of the intensity with respect to the object plane coordinates:

$$\tilde{I}(u) = \int_{-\infty}^{\infty} \exp(2\pi i \frac{x}{M} u) I(x) d(\frac{x}{M}). \quad (10.11)$$

Substituting Equation 10.10 into Equation 10.11 and integrating out $\frac{x}{M}$ first, one can find the following after some tedious derivation (Wu and Liu 2003a):

$$\tilde{I}(u) = \frac{I_0}{M^2} \left\{ \cos\left(\frac{\pi\lambda R_2 u^2}{M}\right) FT[A^2(\eta)] + 2\sin\left(\frac{\pi\lambda R_2 u^2}{M}\right) FT[A^2(\eta)\phi(\eta)] + i\frac{\lambda R_2 u}{M} \sin\left(\frac{\pi\lambda R_2 u^2}{M}\right) FT\left[A(\eta)\frac{dA(\eta)}{d\eta}\right] - 2i\frac{\lambda R_2 u}{M} \cos\left(\frac{\pi\lambda R_2 u^2}{M}\right) FT\left[A(\eta)\frac{dA(\eta)}{d\eta}\phi(\eta)\right] \right\}. \quad (10.12)$$

where $FT[\bullet]$ is the Fourier Transform.

In the derivation of Equation (10.12), we assume both the phase and attenuation vary moderately in a small distance $\lambda R_2 u/M$, such that

$$\begin{aligned} & \exp\left(i\phi(\eta) - i\phi\left(\eta - \frac{\lambda R_2 u}{M}\right)\right) \\ & \approx 1 + i\phi(\eta) - i\phi\left(\eta - \frac{\lambda R_2 u}{M}\right) \end{aligned} \quad (10.13)$$

$$A\left(\eta \pm \frac{\lambda R_2 u}{M}\right) \approx A(\eta) \pm \frac{\lambda R_2 u}{M} \frac{dA(\eta)}{d\eta}. \quad (10.14)$$

These moderate variation conditions are of the forms of Taylor expansions and can easily be satisfied in clinical imaging due to the extremely short wavelength λ of the x-ray and the limited spatial resolution u of the detectors. $\lambda R_2 u/M$ has been estimated to be less than 0.62 micron for a typical mammography system (Wu and Liu 2003a), which is much smaller than the usual size of the breast structures to be imaged. In such cases, the moderate variation conditions can be met. The formula of Equation 10.12 considers the most general cases in clinical applications in a very concise form, providing high flexibility in the implementation of phase retrieval algorithms.

10.2.4 Partial Spatial Coherence and Optical Transfer Functions

To extend the obtained formulations to include the effect of partially coherent and polychromatic x-ray sources and detectors with limited resolution, it is necessary to study the optical transfer function (OTF) of x-ray sources and also that of detectors. The OTF of an x-ray source is closely related to the concept of degree of coherence. The complex degree of coherence (CDC) of an optical wave field (Mandel and Wolf 1995; Goodman 2000) is defined as

$$\mu(x_1, x_2) = \frac{J(x_1, x_2)}{\sqrt{I(x_1)I(x_2)}}, \quad (10.15)$$

where $J(x_1, x_2)$ is the mutual intensity (Mandel and Wolf 1995; Goodman 2000), which is the time-averaged cross-correlation function of the x-ray wave fields at x_1 and x_2 . Note that $J(x, x)$ is just the measured intensity at x . Thus $\mu(x_1, x_2)$ is actually the ratio between the mutual intensity and the measured intensity. Note that $0 \leq |\mu(x_1, x_2)| \leq 1$. When $|\mu(x_1, x_2)| = 1$ for all x_1 and x_2 , the x-ray wave is perfectly spatially coherent, and when $|\mu(x_1, x_2)| = 0$, the x-ray is said to be incoherent. For an intermediate value of $|\mu(x_1, x_2)|$, the x-ray wave is said to be partially coherent.

The CDC for an anode source can be calculated from the van Cittert–Zernike theorem, which states that $\mu(x_1, x_2)$ is a

scaled FT of the x-ray intensity distribution $I_s(x)$ at the source surface (Mandel and Wolf 1995):

$$\mu(x_1, x_2) = \exp\left(i\pi \frac{x_1^2 - x_2^2}{\lambda R_1}\right) \tilde{\mu}(x_1 - x_2), \quad (10.16)$$

where

$$\tilde{\mu}\left(\frac{\lambda R_2 u}{M}\right) = \frac{\int I_s(x) \exp(i2\pi x \frac{(M-1)u}{M}) dx}{\int I_s(x) dx}. \quad (10.17)$$

In the literature, any source for which the CDC $\mu(x_1, x_2)$ can be written in the form as shown in Equation 10.16 is called a Schell-model source. Therefore, the van Cittert–Zernike theorem shows that anode sources are Schell-model sources (Mandel and Wolf 1995). It should be stressed that $\mu(x_1, x_2)$ in Equation 10.16 depends only on the difference vector $(x_1 - x_2)$. To emphasize this special feature of $\tilde{\mu}(x_1 - x_2)$, we call it the reduced complex degree of coherence (RCDC).

The effects of the finite focal spot size can also be described by its optical transfer function for the geometric unsharpness $\text{OTF}_{\text{G.U.}}(u/M)$. If the focal spot is a uniform circular disk of diameter f , the modulus of $\text{OTF}_{\text{G.U.}}(u/M)$ is given by

$$\left| \text{OTF}_{\text{G.U.}}\left(\frac{u}{M}\right) \right| = \frac{2J_1[\pi f(M-1)|u|/M]}{\pi f(M-1)|u|/M}, \quad (10.18)$$

where $J_1(x)$ is a Bessel function of the first kind. Substituting the circular focal spot into Equation 10.17 as a 2-D function and computing the scaled Fourier transform using the circular symmetry, one will realize that

$$\begin{aligned} \tilde{\mu}\left(\frac{\lambda R_2 u}{M}\right) &= \frac{2J_1[\pi f(M-1)|u|/M]}{\pi f(M-1)|u|/M} \\ &= \text{OTF}_{\text{G.U.}}\left(\frac{u}{M}\right). \end{aligned} \quad (10.19)$$

The above result is based on the notion that the image generated by an anode source can be obtained by summing over the intensities generated by each individual source point in the anode (Goodman 2000), and provides a theoretical understanding of the relation between partial spatial coherence of the incident x-ray wave from a focal spot and the OTF for the geometric unsharpness associated with a finite focal spot.

Now let us consider the effect of detectors with limited resolution, i.e., with pixels of a finite size. For a detector with an active pixel size p_{ax} (determined by the pixel pitch and the

fill factor of the detector), the modulus of its OTF is given by (Quandji et al. 2002)

$$\left| \text{OTF}_{\text{det}}\left(\frac{u}{M}\right) \right| = \text{sinc}\left(\frac{p_{ax}u}{M}\right). \quad (10.20)$$

Equations 10.17 and 10.20 constitute the theoretical model of the effects of the partial coherence of the x-ray sources, and the limited resolution of the detectors. This model will be taken into consideration when we present a full theory for phase-contrast imaging in the following derivations.

10.2.5 A Full Phase-space Theoretical Framework

In this section, we will extend the formulations for ideal imaging systems to include the effects of non-ideal x-ray sources and detectors by using the Wigner distribution. Originally developed for quantum mechanics, the Wigner distribution also provides a useful phase-space formalism for optics (Mandel and Wolf 1995). While in quantum mechanics the Wigner distribution is the Moyal transform of the configuration space–density matrix, in optics it is the Moyal transform of the two-point cross spectral density of the x-ray wave field (Littlejohn 1986). For the sake of convenience, we define the Wigner distribution $W(x, u; z)$ as

$$W(x, u; z) = \int J(x + q/2, x - q/2; z) \times \exp(-i2\pi qu) dq, \quad (10.21)$$

where $J(x_1, x_2; z)$ is the mutual intensity of the wave fields at distance z from the source plane, q is the displacement variable, and u is the spatial frequency variable. The advantages of adopting the Wigner distribution are twofold. First, with the statistical nature of the Wigner distribution, we can incorporate more accurately the partial coherence of the x-ray wave field into the theory. Second, the evolution of the Wigner distribution in the phase space is much easier to handle than the wave field itself due to its affine canonical covariance in phase space, as will be explained below.

Consider the x-ray wave paraxial evolution from the exit of the object at $z = R_1$ to the entrance of the imaging detector at $z = R_1 + R_2$. During the evolution, the Wigner distribution satisfies the free Louville equation in the phase space (Littlejohn 1986):

$$\frac{\partial W}{\partial z} + \lambda u \frac{\partial W}{\partial x} = 0. \quad (10.22)$$

Let us denote the Wigner distribution at $z = R_1$ as $W(x, u; R_1)$. Using $W(x, u; R_1)$ as the initial condition and solving Equation 10.22, we find the solution for $W(x, u; z)$:

$$W(x, u; z) = W[x - \lambda(z - R_1)u, u; R_1]. \quad (10.23)$$

Combining Equation 10.23 and the definition of the Wigner distribution, we find the x-ray intensity at the detector plane to be

$$I(x; R_1 + R_2) = \int W(x, u; R_1 + R_2) du = \int W(x - \lambda R_2 u, u; R_1) du. \quad (10.24)$$

After a tedious derivation, we obtain the FT of the x-ray intensity at detector plane ($z = R_1 + R_2$), as given by

$$\begin{aligned} \tilde{I}(u; R_1 + R_2) &= FT[I(x; R_1 + R_2)] \\ &= \int J\left(\eta + \frac{\lambda R_2 u}{2}, \eta - \frac{\lambda R_2 u}{2}\right) \\ &\times T\left(\eta + \frac{\lambda R_2 u}{2}\right) T^*\left(\eta - \frac{\lambda R_2 u}{2}\right) \exp(i2\pi\eta u) d\eta. \end{aligned} \quad (10.25)$$

By using RCDC, the mutual intensity of a uniform incident radiation can be written as

$$\begin{aligned} J(x_1, x_2) &= I_0 \mu(x_1, x_2) \\ &= I_0 \exp\left(i\pi \frac{x_1^2 - x_2^2}{\lambda R_1}\right) \tilde{\mu}(x_1 - x_2). \end{aligned} \quad (10.26)$$

Substituting the mutual intensity into Equation 10.25 and taking the imaging detector’s response into consideration, we discover that

$$\begin{aligned} \tilde{I}(u; R_1 + R_2) &= I_0 \text{OTF}_{\text{G.U.}}\left(\frac{u}{M}\right) \text{OTF}_{\text{det}}\left(\frac{u}{M}\right) \\ &\times \int T\left(\eta + \frac{\lambda R_2 u}{2}\right) T^*\left(\eta - \frac{\lambda R_2 u}{2}\right) \exp(i2\pi\eta u) d\eta \end{aligned} \quad (10.27)$$

Following the same derivation as Equation 10.12, we obtain:

$$\begin{aligned} \tilde{I}(u) &= \frac{I_0}{M^2} \text{OTF}_{\text{G.U.}}\left(\frac{u}{M}\right) \text{OTF}_{\text{det}}\left(\frac{u}{M}\right) \\ &\left\{ \cos\left(\frac{\pi\lambda R_2 u^2}{M}\right) FT[A^2(\eta)] \right. \\ &+ 2 \sin\left(\frac{\pi\lambda R_2 u^2}{M}\right) FT[A^2(\eta)\phi(\eta)] \\ &+ i \frac{\lambda R_2 u}{M} \sin\left(\frac{\pi\lambda R_2 u^2}{M}\right) FT\left[A(\eta) \frac{dA(\eta)}{d\eta}\right] \\ &\left. - i 2 \frac{\lambda R_2 u}{M} \cos\left(\frac{\pi\lambda R_2 u^2}{M}\right) FT\left[A(\eta) \frac{dA(\eta)}{d\eta} \phi(\eta)\right] \right\}. \end{aligned} \quad (10.28)$$

Equation 10.28 is a central result of our theoretical framework. It shows the effects on the phase-contrast image formation of not only the x-ray attenuation and detector resolution, but also the changes in the spatial coherence and wavefront curvature of x-ray during x-ray propagation. It holds true not only for x-rays from anode sources, but also for general x-ray sources such as undulators. To avoid aliasing effects, Equation 10.28 holds only for the spatial frequencies below the Nyquist frequency u_{Nyquist} as determined by the pixelation of the detector, and we assume that the object is band-limited within Mu_{Nyquist} .

By further assuming $A(\eta) \approx A(\eta \pm \lambda R_2 u/M)$, we have

$$\begin{aligned} \tilde{I}(u) = & \frac{I_0}{M^2} \text{OTF}_{\text{G.U.}}\left(\frac{u}{M}\right) \text{OTF}_{\text{det}}\left(\frac{u}{M}\right) \\ & \times \left\{ \cos\left(\frac{\pi\lambda R_2 u^2}{M}\right) FT[A^2(\eta)] \right. \\ & \left. + 2 \sin\left(\frac{\pi\lambda R_2 u^2}{M}\right) FT[A^2(\eta)\phi(\eta)] \right\}, \end{aligned} \quad (10.29)$$

and by considering that in clinical applications $\pi\lambda R_2 u^2/M \ll 1$, we obtain

$$\begin{aligned} \tilde{I}(u) = & \frac{I_0}{M^2} \text{OTF}_{\text{G.U.}}\left(\frac{u}{M}\right) \text{OTF}_{\text{det}}\left(\frac{u}{M}\right) \\ & \times \left\{ FT[A^2(\eta)] + \frac{2\pi\lambda R_2 u^2}{M} FT[A^2(\eta)\phi(\eta)] \right\}. \end{aligned} \quad (10.30)$$

Now let us take into consideration the polychromatism of the x-ray sources. Using Equation 10.7, we rewrite Equation 10.30 as

$$\begin{aligned} \tilde{I}(u) = & \frac{I_0}{M^2} \text{OTF}_{\text{G.U.}}\left(\frac{u}{M}\right) \text{OTF}_{\text{det}}\left(\frac{u}{M}\right) \\ & \times \left\{ FT[A^2(\eta)] - \frac{2\pi\lambda^2 R_2 u^2 r_e}{M} FT[A^2(\eta)\rho_{e,p}(\eta)] \right\}, \end{aligned} \quad (10.31)$$

Averaging this equation over x-ray spectrum yields, after appropriate approximations, gives the following formula:

$$\begin{aligned} \tilde{I}(u) = & \frac{I_0}{M^2} \\ & \times \left\{ \text{OTF}_{\text{G.U.}}\left(\frac{u}{M}\right) \text{OTF}_{\text{det}}\left(\frac{u}{M}\right) FT[\langle A^2 \rangle(\eta)] \right. \\ & \left. - 2r_e \text{RPF}(u) FT[\langle A^2 \rangle \rho_{e,p}(\eta)] \right\}, \end{aligned} \quad (10.32)$$

where $\langle A^2 \rangle$ denotes the total transmission of the object to the incident polychromatic x-ray (i.e., the attenuation image) and

$\rho_{e,p}$ is the projected electron density. Note that from Equation 10.7 the projected phase map ϕ is proportional to the projected electron density map $\rho_{e,p}$. The relative phase-contrast factor (RPF(u)) is given by

$$\begin{aligned} \text{RPF}(u) = & c^2 h^2 \text{OTF}_{\text{G.U.}}\left(\frac{u}{M}\right) \\ & \times \text{OTF}_{\text{det}}\left(\frac{u}{M}\right) \int \frac{\pi R_2 u^2}{ME^2} S_{\text{Exit}}(E) dE \end{aligned} \quad (10.33)$$

where h is Plank's constant, c is the speed of light, and $S_{\text{Exit}}(E)$ is the normalized spectrum of the average exiting beam.

The above results can be generalized to the 2D case as well, where Equation 10.29 becomes

$$\begin{aligned} \tilde{I}(u, v) = & \frac{I_0}{M^2} \text{OTF}_{\text{G.U.}}\left(\frac{u}{M}, \frac{v}{M}\right) \text{OTF}_{\text{det}}\left(\frac{u}{M}, \frac{v}{M}\right) \\ & \times \left\{ \cos\left(\frac{\pi\lambda R_2 (u^2 + v^2)}{M}\right) FT[A^2] \right. \\ & \left. + 2 \sin\left(\frac{\pi\lambda R_2 (u^2 + v^2)}{M}\right) FT[A^2 \phi] \right\}, \end{aligned} \quad (10.34)$$

Equation 10.32 becomes

$$\begin{aligned} \tilde{I}(u, v) = & \frac{I_0}{M^2} \left[\text{OTF}_{\text{G.U.}}\left(\frac{u}{M}, \frac{v}{M}\right) \text{OTF}_{\text{det}}\left(\frac{u}{M}, \frac{v}{M}\right) \right. \\ & \left. \times FT[\langle A^2 \rangle] - 2r_e \text{RPF}(u, v) FT[\langle A^2 \rangle \rho_{e,p}] \right], \end{aligned} \quad (10.35)$$

and Equation 10.33 becomes

$$\begin{aligned} \text{RPF}(u, v) = & c^2 h^2 \text{OTF}_{\text{G.U.}}\left(\frac{u}{M}, \frac{v}{M}\right) \\ & \times \text{OTF}_{\text{det}}\left(\frac{u}{M}, \frac{v}{M}\right) \int \frac{\pi R_2 (u^2 + v^2)}{ME^2} S_{\text{Exit}}(E) dE. \end{aligned} \quad (10.36)$$

Equations 10.35 and 10.36 quantify the effects of partial spatial coherence, polychromatic spectrum, body attenuation, image detector resolution, and radiation dose on the phase-contrast visibility. From equations 10.35 and 10.36, the modulus of Relative Phase-contrast Factor ($|\text{RPF}(u, v)|$) provides a figure of merit for the transfer of the object's phase contrast to an image. More accurately, the modulus of RPF(u, v) indicates the level of phase contrast that is transferred by the x-ray imaging system at a given spatial frequency (u, v). The larger

Table 10–1: Differences between the phase-contrast image and the phase image of an object (Reprinted from Wu and Liu 2007a)

Notation	Phase-contrast Image I_{pc}	Phase Image $\phi(x,y)$
Formation	Interference between waves of different phase shifts.	Retrieved from an acquired attenuation image I_{ab} and phase-contrast image I_{pc}
Property	The edge enhancement increases with the Laplacian and gradient of phase shift $\phi(x,y)$ and with increasing coherence degree of the x-ray.	$\phi(x,y)$ yields a map $\rho_{e,p}(x,y)$ of projected electron densities, which are the intrinsic attributes of the object
Detector configuration	One detector placed a distance downstream from the object to allow for wave diffraction; either screen/film detector or a digital detector.	In our approach, two detectors are used: the first detects a portion of radiation to form an attenuation image, while allowing the rest of the radiation to reach the second detector to form a phase-contrast image, and the two images are used for the phase retrieval. The two detectors are balanced for optimal phase retrieval with reasonable radiation dose.
Images acquired	One exposure acquires a single phase-contrast image.	With the dual-detector technique, a single exposure results in three images of a given object: two acquired images I_{ab} and I_{pc} , plus a retrieved phase image $\phi(x,y)$.
Optical measurements and phase-retrieval algorithm development	N.A.	Intended to measure the coherence degree, the detector's optical transfer function, and the spectral average $\langle \lambda^2 \rangle$ to further the development of robust phase-retrieval algorithms.
Clinical significance	I_{pc} provides an edge enhancement effect from tissue phase contrast, thereby improving the image data's diagnostic quality.	$\phi(x,y)$ provides a map of tissue projected electron densities, and therefore a quantitative tissue characterization. Combined with tomographic image data, the 3D map of the object's electron densities becomes available for tissue structural characterization and visualization.

the $|RPF(u,v)|$, the better the feature visibility of phase contrast. Note that RPF depends not only on the focal spot size, shape, and geometry and the detector resolutions, but also on the exiting x-ray spectrum $S_{Exit}(E)$. The exiting spectrum $S_{Exit}(E)$ differs from the incident x-ray spectrum in that it represents the x-ray beam hardening effect on phase contrast. Thus these equations can be used to provide design guidelines for general in-line phase-contrast imaging systems, which is the topic of Section 10.3.

10.2.6 Phase-contrast Imaging vs. Phase Retrieval

Phase-contrast imaging is a technology that uses the phase change to enhance the total image contrast. To obtain phase information, a distance of propagation is needed to allow for wave diffraction, i.e., the superposition of sub-waves. In this case, the overall image intensity contrast comes from both phase and attenuation. The detected signal in the image contains information about the phase difference between sub-waves, which reflects different phase shifts induced by the subject, not the phase itself. As discussed in depth previously, the phase contrast in I_{pc} is affected by the phase-shift $\phi(x,y)$ and the attenuation $A^2(x,y)$ through a very complicated mechanism. It is also affected by the coherence degree of the x-ray source, and the detector's spatial frequency response. Therefore, the contrast enhancement provides only qualitative information about the tissue structure. However, phase-con-

trast imaging theories show explicitly how the image relies on the attenuation and phase shift together with other experimental parameters, and thus serve as a theoretical framework for phase retrieval.

In contrast to phase-contrast projection acquisition, phase retrieval is a numerical method for retrieving the quantitative phase map $\phi(x,y)$ from the phase-contrast images. From $\phi(x,y)$, one can easily derive a map of the object's projected electron densities $\rho_{e,p}(x,y)$. Since electron density is an intrinsic attribute of the object, the map $\rho_{e,p}(x,y)$ yields a quantitative image of the object's structure. Moreover, in phase-contrast tomography it is necessary to perform phase retrievals in order to reconstruct quantitative artifact-free tomograms. In principle, phase-contrast x-ray tomography can be performed by applying standard tomography reconstruction methods such as filtered backprojection directly onto phase-contrast angular projections to obtain 3D tomograms. Phase-sensitive tomograms reconstructed in this manner exhibit enhanced interfaces between the layers of different materials and tissues, and thus are not maps of the linear attenuation coefficients (LACs) of the sample, but are instead maps of the reconstructed apparent LACs, which may present anomalously large or even negative apparent LAC values at interfaces between different materials and tissues. These "artifacts" may cause faulty interpretation of the imaged subject (Wu et al. 2008). However, if phase retrieval is performed

for each phase-contrast projection image before the tomographic reconstruction, an accurate 3D distribution of electron density can be generated without the aforementioned artifacts.

In short, phase-contrast imaging is the forward process of producing an image with phase enhancement, while phase retrieval is the inverse problem of deriving quantitative information about the object from the image data. The differences between the two phase-sensitive imaging modalities are summarized in Table 10–1 (Wu and Liu 2007a).

10.3 Design Considerations and Clinical Implementation of In-line X-ray Phase-sensitive Imaging

10.3.1 Coherence Requirement in the Clinical Implementation of Phase-contrast Imaging

It is well known that interference patterns occur only if the waves in superposition are coherent. An understanding of the coherence requirement is especially critical for the clinical implementation of phase-sensitive imaging, since the anode source used in clinical imaging is an incoherent source. To exhibit phase contrast, the x-ray wave illuminating the object should be at least partially coherent. The partial coherence of the illuminating wave from a finite source of size s is specified in terms of the lateral coherence length L_{\perp} (Wu and Liu 2003b; Wu and Liu 2007a):

$$L_{\perp} = \lambda R_1 / s. \quad (10.37)$$

L_{\perp} is the linear size of a region over which the wave field is strongly correlated, and it is roughly the maximal separation of two points for which the interference occurs. For instance, the inter-slit separation in a Young's double-slit experiment should be less than L_{\perp} for visible interference fringes. One should note that the lateral coherence length L_{\perp} is defined exactly for narrow-band x-rays, because L_{\perp} is derived from the study of mutual intensity and the coherence degree of quasi-monochromatic waves. But since the cross-spectral densities of a polychromatic x-ray obey the same propagation laws as the mutual intensity does, Equation 10.37 holds for cases of the polychromatic x-ray as well. Note that the cross-spectral density is defined as the ensemble average of the conjugated product of wave amplitudes at two positions for a given x-ray frequency. It measures the statistical similarity (spatial coherence) of the x-ray wave fields at the two positions. For a quasi-monochromatic x-ray, cross-spectral density is called the mutual intensity.

In practice, one needs to know how large L_{\perp} must be in order to achieve phase-contrast visibility. In the literature there are confusing statements regarding this. For example, one statement in the literature claims that in order to exhibit visible phase contrast in an image, the lateral coherence length L_{\perp} should be roughly equal to the length of one dark–

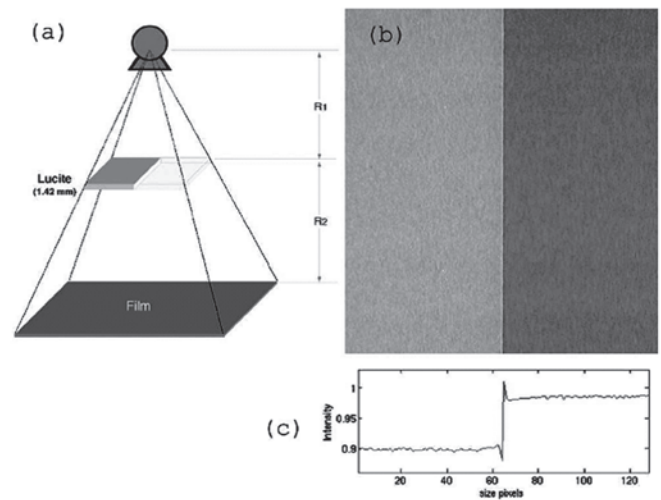


Figure 10–4. a) Schematic of the phase-contrast imaging of an acrylic edge phantom. b) Acquired phase-contrast image of the acrylic edge phantom. c) Intensity profile across the step edge in b). (From Wu and Liu 2007a.)

bright fringe pair. According to this claim, for a phase-contrast fringe of size about $50 \mu\text{m}$, as encountered for clinical imaging, the lateral coherent length L_{\perp} of the incident x ray should be about $50 \mu\text{m}$. However, due to small x-ray wavelengths, L_{\perp} is generally much smaller than this suggested size. For example, if an x-ray of 18.5 keV is emitted from a focal spot of $50 \mu\text{m}$, with a source–object distance R_1 of 1 m, the resulting lateral coherent length is $1.34 \mu\text{m}$. One needs a tremendously long source–object distance R_1 of 40 m to achieve an assumed L_{\perp} of $53.6 \mu\text{m}$. Such long source–object distances are obviously not practical in a clinical imaging setting, due to both space constraints and flux requirements. Therefore, if the aforementioned lateral coherence length requirement for phase-sensitive imaging was true, clinical applications of phase-contrast imaging would not be worth pursuing.

Fortunately the claim is incorrect, and it is in contradiction with experimental results as well. To justify this claim, we performed the following experiment (Wu and Liu 2003b). As shown in Figure 10–4a, a laser-cut acrylic plate edge of 1.42 mm thickness was imaged with an x-ray tube containing a $14 \mu\text{m}$ focal spot and average photon energy of 18.5 keV. The SID = 178 cm and $R_2 = 111.9 \text{ cm}$, hence the magnification factor $M = 2.7$. The amount of phase shift across the acrylic plate calculated by Equation 10.7 is 30.5π . Figure 10–4b shows the resultant image, which clearly exhibits edge enhancement features near the step edge in the form of dark and bright strips immediately adjacent to the shelf, the signature enhancement pattern of a phase step. Correspondingly, the intensity profile across the edge demonstrates the expected upward- and downward-overshooting at the boundary. Clearly, the lateral coherence length requirement claimed in

previous literature is violated in this experiment, as the width of the dark–bright fringe pair in the image is much larger than the calculated L_{\perp} for this setup (3.16 μm).

The problem with the lateral coherence length assumption is that it fails to take into account the x-ray diffraction from the object's exit to the detector. Considering this diffraction process, we found that what really determines phase contrast visibility is not solely the lateral coherence length L_{\perp} . Rather, for a structural component of the object with spatial frequency u , its visibility is, among other things, proportional to the modulus of RCDC, as is proved in Section 10.2. From Equation 10.23 one can see that the wave diffraction in free space over a distance R_2 from the object's exit to the detector entrance is simply created by a phase-space shearing; the photon density distribution at x is replaced by that at position $(x - \lambda R_2 u / M)$, referring to the object plane. The phase-space shearing leads to wave superposition when forming the phase contrast, hence the coherence criteria for phase-sensitive imaging should be the size of the phase-space shearing compared to the lateral coherence length L_{\perp} . We call the size of the phase-space shearing the shearing length L_{shear} , which is given by

$$L_{\text{shear}} = \frac{\lambda R_2 |u|}{M} \quad (10.38)$$

From the above analysis we note that it is the ratio $L_{\text{shear}} / L_{\perp}$, rather than L_{\perp} alone, that determines the coherence effects on the phase-contrast visibility of the object's frequency u component. From Equations 10.37 and 10.38, the ratio $L_{\text{shear}} / L_{\perp}$ is given by (Wu and Liu 2007a):

$$\frac{L_{\text{shear}}}{L_{\perp}} = \frac{R_2 s |u|}{MR_1} = \frac{(M-1)s |u|}{M}. \quad (10.39)$$

Note that $L_{\text{shear}} / L_{\perp}$ is wavelength independent, since both L_{\perp} and L_{shear} are proportional to λ . For a given object structural component of frequency u , if $L_{\text{shear}} / L_{\perp} \ll 1$, the wave field is almost fully coherent over the shearing length, and the phase contrast associated with this structure component is visible. On the other hand, if $L_{\text{shear}} / L_{\perp} \geq 1$, the wave field is incoherent over the shearing length, and the phase contrast associated with this structure component is invisible. For intermediate cases with $L_{\text{shear}} / L_{\perp} < 1$, the wave field is almost partially coherent, and phase-contrast visibility increases with decreasing L_{shear} for a given object structural component of frequency u .

Applying this concept to the case described by Figure 10–4, equations 10.37, 10.38, and 10.39 can be used to show that the ratio $L_{\text{shear}} / L_{\perp} = 0.176$ for a high-frequency component of $|u| = 20$ lp/mm. This explains why one can see the phase contrast manifesting as edge enhancement in Figure 10–4b, while the computed lateral coherence length L_{\perp} alone suggests otherwise. Hence it is demonstrated that the ratio

$L_{\text{shear}} / L_{\perp}$ provides a simple but good measure of the coherence degree realized in a phase-sensitive imaging system. For an anode source containing a uniform focal spot, this ratio is related to the modulus of $\text{OTF}_{\text{G.U.}}(u/M)$ or RCDC by (Wu and Liu 2007a)

$$\left| \text{OTF}_{\text{G.U.}} \left(\frac{u}{M} \right) \right| = \frac{2J_1(\pi L_{\text{shear}} / L_{\perp})}{\pi L_{\text{shear}} / L_{\perp}} \quad (10.40)$$

10.3.2 Analysis Based Upon Relative Phase Factor (RPF)

Equations 10.35 and 10.36 quantify the effects of partial spatial coherence, polychromatic spectrum, body attenuation, image detector resolution, and radiation dose on the phase-contrast visibility, and can be used to provide design guidelines for general in-line phase-contrast imaging systems, including clinical systems. The larger the modulus of $\text{RPF}(u, v)$, the more the phase contrast manifests. Now we can calculate RPF for a typical imaging system while varying configuration parameters to aid in system design. As an example, we consider the application of RPF analysis in phase-contrast mammography. Here we study the important relationships between system geometry, detector resolution, the size and radiation output of the x-ray source, and patient dose in phase-contrast imaging (Wu and Liu 2003b).

Computer Simulation of the RPF for Mammography as a Function of System Design

From the discussion of the coherence requirements, it is clear that an x-ray tube for clinical phase-contrast mammography should have a small but bright focal spot. A conventional x-ray tube for 2D mammography provides a small focal spot of about 0.1 mm and a tube current of 25–35 mA operating at 24–35 kV. We will show by using the RPF analysis in this section that an x-ray tube consisting of a molybdenum (Mo) target with a focal spot of 0.025 mm and a tube current of 25 mA will adequately balance the need for spatial coherence and sufficient x-ray output flux with an SID of 1 m.

Let us assume the clinical condition of a 50% adipose and 50% glandular breast of 5 cm thickness, and an infiltrating ductal carcinoma lesion with a diameter and thickness of 0.5 cm. This lesion represents a clinically relevant breast cancer detection task.

From Equation 10.36 it is clear that R_2 cannot be too small. If R_2 were equal to zero, the phase-contrast information would be completely lost, as a diffracted beam has to travel a sufficient lateral distance to reveal any phase change effects. As the ratio R_2 / M increases, RFP increases as well, until the sine-factor in Equation 10.29 reaches its maximum. Therefore, Equation 10.36 suggests that a large R_2 would be favored for increasing the imaged phase contrast. On the other hand, note that the image magnification factor M may increase with

Table 10–2: Design parameters of a proposed screen-film-based phase-contrast x-ray imaging system
(Reprinted from Wu and Liu 2003b)

Source to object and detector-1, R_1 (m)	0.60	0.50	0.60
Object–detector-2, R_2 (m)	0.40	0.30	0.40
Source to detector distance (m)	1.00	0.80	1.00
Magnification $(R_1 + R_2)/R_1$	1.67	1.60	1.67
Target frequency (lp/mm)	20.00	20.00	20.00
X-ray focal spot size (mm)	0.025	0.025	0.025
X-ray kV	30	25	25
Tube target/filter	Mo/Mo	Mo/Mo	Mo/Mo
HVL (mm) Al	0.382	0.32	0.32
att-CNR	135.52	170.94	170.94
Entrance skin exposure (R)	1.220	1.897	2.058
Patient absorbed dose (mrad)	198.15	254.45	276.10
Relative phase-contrast factor at target frequency (\AA)	1.95 E-02	1.83 E-02	2.30 E-02
Exposure time at 25 mA (s)	3.63	6.27	9.80

(Considering a 5 cm, 50% glandular / 50% adipose breast thickness, and an infiltrating ductal carcinoma of 0.5 cm in diameter and thickness, without a Bucky grid).

R_2 as well. An increase of M will affect RFP via the terms R_2/M and OTF. In this study we restrict the magnification factor such that it will not exceed 2, in conformance with current mammography practices. For convenience of operation (breast positioning and breast compression), we designed the SID to be about 1 m, not much larger than the conventional SID of about 0.65 m. It should be noted that a selection of R_1 and R_2 will influence not only the imaged phase contrast, but also a series of other factors, such as the consistency of the spatial resolution matching between the detector and the target, scatter suppression, average glandular dose to the breast, and the exposure time. For example, for a fixed R_1 , a large R_2 could allow a reduction of the average glandular doses deposited to the breast by omission of an anti-scatter grid, but the magnification factor M and exposure time would increase. An increase in M could affect the imaged phase contrast as predicted by Equation 10.35, and an increase in the exposure time could lead to motion blur of the image. In order to optimally balance the many correlated factors of phase-contrast mammography in a design analysis, we have performed computer simulations as described below (Wu and Liu 2003b).

From Equation 10.34, the phase contrast manifests at higher frequencies than attenuation-based contrast. Hence, in the simulation we calculated the RPF at an object–plane target frequency that is matched with the adopted detector resolution and magnification factor. For example, for a full field flat panel detector with a pixel pitch of 70 μm , we set the target frequency according to the maximum spatial frequency of the

detector, 7.1 lp/mm, adjusted for the magnification factor M . For a screen/film detector such as the Kodak 2000 film/screen system, we set the target frequency at 20 lp/mm regardless of the magnification factor M adopted. The modulus of the RPF from Equation 10.36 was calculated for these frequencies, with the assumption that a larger $|RPF(u,v)|$ results in better feature visibility from the phase-contrast process.

For clinical phase-contrast imaging, it is desirable to preserve as much attenuation-based tissue–lesion contrast as possible; hence, we assumed a Mo target and a 30 μm thick Mo filter for the x-ray tube. The exposure in the simulation was selected in such a way that the conventional attenuation-based contrast-to-noise ratio (att-CNR) was maintained at the standard level for conventional mammography. Exposure parameters such as the attenuation-based CNR, the average glandular dose to breast, and necessary exposure time were derived from the computer simulation. In the simulation, the x-ray spectral model for the Mo/Mo target/filter assembly was based on a successful semi-empirical model of the x-ray spectra for mammography (Tucker et al. 1991). The average glandular doses were calculated according to the normalized average glandular doses derived from Monte Carlo simulations (Wu et al. 1991). No Bucky grid was assumed in the simulation because of the large air gap employed in phase-contrast x-ray imaging.

The phase-contrast visibility at a target spatial frequency of 20 lp/mm was simulated as a function of system design parameters, including R_1 , R_2 , and magnification M . Other operating parameters, including x-ray exposure and x-ray focal spot size, were also included. The results of the simula-

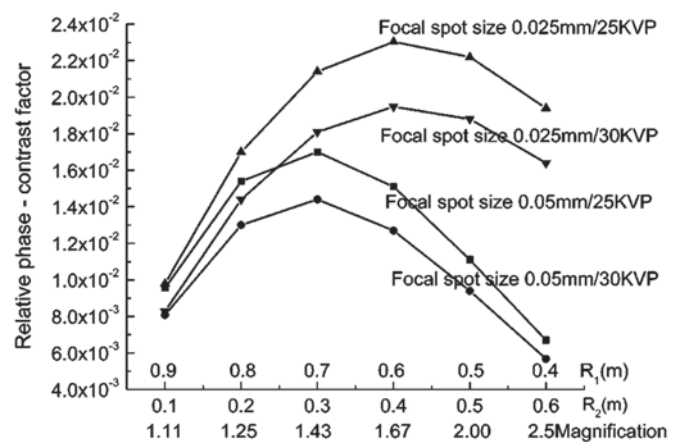


Figure 10–5. Average moduli of the RPF versus system design parameters (R_1 , R_2 , and M). R_1 is the source to object distance, R_2 is the object to detector distance, and M is the magnification ratio. Two different focal spot sizes (0.025 and 0.05 mm) and two different x-ray energies (25 and 30 kV) were used. Target frequency = 20 lp/mm. (From Wu and Liu 2003b.)

Table 10–3: Design parameters of a proposed digital detector based phase-contrast x-ray imaging system
(Reprinted from Wu and Liu 2003b)

Source to object R_1 (m)	0.60	0.50	0.60	0.50	0.40
Object–detector-2, R_2 (m)	0.40	0.50	0.40	0.30	0.60
Source to detector distance (m)	1.00	1.00	1.00	0.80	1.00
Magnification $(R_1 + R_2)/R_1$	1.67	2.00	1.67	1.60	2.50
Digital detector pixel pitch (mm)	0.07	0.07	0.07	0.07	0.07
Target frequency (lp/mm)	11.9	14.3	11.9	11.4	17.9
Focal spot size (mm)	0.025	0.025	0.025	0.025	0.025
X-ray kV	30	30	25	25	30
Tube target/filter	Mo/Mo	Mo/Mo	Mo/Mo	Mo/Mo	Mo/Mo
HVL (mm) Al	0.382	0.382	0.32	0.32	0.382
att-CNR	135.52	135.5	170.94	170.94	135.5
Entrance skin exposure (R)	1.220	1.757	2.058	1.897	2.745
Patient absorbed dose (mrad)	198.15	285.30	276.10	254.45	445.80
Relative phase-contrast factor at target frequency (\AA)	7.53E-03	1.06E-02	8.90E-03	6.47E-03	1.39E-02
Exposure time at 25 mA (s)	3.63	3.63	9.80	6.27	3.63

(Considering a 5 cm, 50% glandular / 50% adipose breast thickness, and an infiltrating ductal carcinoma of 0.5 cm in diameter and thickness, without a Bucky grid).

tion are summarized in figures 10–5 and 10–6, and in tables 10–2 and 10–3 (Wu and Liu 2003b).

The simulations reveal several important aspects of phase-contrast mammography. First, as is shown in Figure 10–5, the RPF moduli increase with the object-to-detector distance R_2 and the magnification M only up to a certain M , after which they decrease due to reduced x-ray spatial coherence. Based on the results in Figure 10–5, the optimal RPF

moduli will be achieved with a magnification of around $M = 1.67$ for a 0.025 mm focal spot. We note that the optimal RPF moduli for a 0.05 mm focal spot will be achieved at a lower magnification of around $M = 1.43$ due to the degraded source spatial coherence. Moreover, the optimal RPF moduli for a 0.05 mm focal spot are substantially (approximately 35%) lower than those for a 0.025 mm focal spot. The effect of kV on RPF can be noted as well from Figure 10–5. A lower kV results in higher RPF values. However, although the RPF values in Figure 10–5 favor 25 kV over 30 kV, the results in Figure 10–6 indicate that higher average glandular doses would be required if 25 kV were used. It should also be noted, though, that the calculated radiation dose levels for the simulated 5 cm breast with 50% adipose and 50% glandular tissue composition are in a range that is clinically acceptable.

To demonstrate the design guidelines and trade-offs, tables 10–2 and 10–3 give three specific settings for the same imaging task specified earlier. Table 10–2 is for a Kodak 2000 mammography screen/film system, and Table 10–3 shows the settings for a flat panel detector with 0.07 mm pixel pitch. These parameters are derived through computer simulations described in the previous section. An optimal design should balance a high RPF and att-CNR with an acceptable exposure time and associated average glandular dose to breast. For a 5-cm breast of 50% adipose and 50% glandular tissue, an exposure time no larger than 4 s is definitely acceptable from the point of view of reducing motion artifacts. As for the radiation doses involved in the phase-contrast mammography, tables 10–2 and 10–3 show that while the att-CNR values are comfortably high, the average glandular doses in most cases are less than 300 mrad, lower than that for a 5-cm-thick breast of

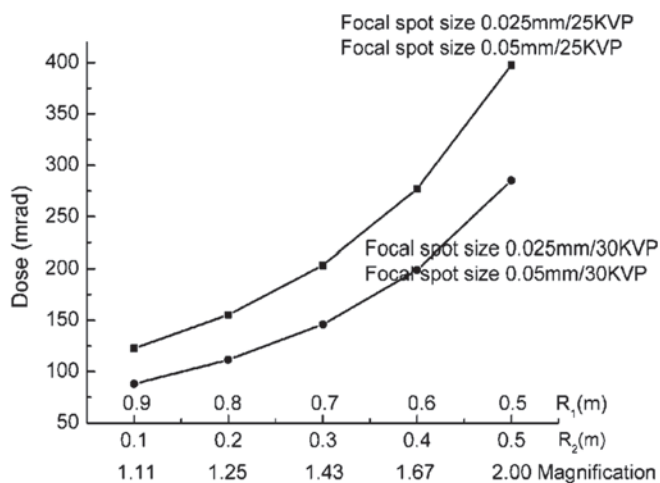


Figure 10–6. Breast average glandular dose versus system design parameters (R_1 , R_2 , and M). R_1 is the source to object distance, R_2 is the object to detector distance, and M is the magnification ratio. Two different focal spot sizes (0.025 and 0.05 mm) and two different x-ray energies (25 and 30 kV) were used. (From Wu and Liu 2003b.)

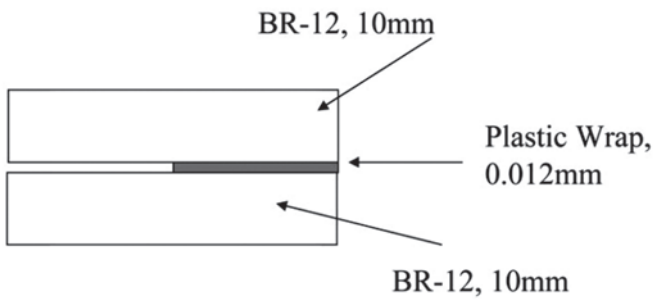


Figure 10–7. A phantom in x-ray phase contrast imaging experiments. (From Wu and Liu 2003b.)

50% adipose and 50% glandular tissue in conventional mammography. We noted that the film-based system provides higher detector resolution and, therefore, it could offer a higher relative phase contrast factor than the digital system (referring to tables 10–2 and 10–3). However, film-based images are limited in dynamic range: their gamma curves are nonlinear and affected by many factors such as the film processing chemistry and parameters. Therefore, film-based images may be less accurate for phase retrieval than digitally acquired images. Accordingly, the effect of the phase contrast may be better visualized by human observers using digitally acquired images.

Experimental Validation of the RPF Analysis

Experiments were performed to validate the proposed phase-contrast x-ray imaging theory and to test the sensitivity of the in-line phase-contrast imaging (Wu and Liu 2003b). The

experimental setup employed a conventional tungsten target x-ray tube with a 0.02 mm focal spot. The x-ray tube was run at 0.3 mA and 30 kV. A digital x-ray detector with 1024-by-1024 pixels and 0.048 mm pixel pitch was positioned at 57.2 cm from the x-ray source. A phantom was placed at several different locations between the x-ray source and the detector, yielding varying combinations of R_1 and R_2 , and thus M . The phantom consisted of two 1-cm-thick BR-12 breast-equivalent slabs, with plastic wraps of 0.12 mm thickness sandwiched between the slabs (Figure 10–7). A series of phantom images were acquired with detector entrance exposures in the range of 10 to 13 mR. Standard flat field correction procedures were performed before images were presented and analyzed.

As seen in the images of Figure 10–8b and Figure 10–9, when $M=1.54$, a sharp edge is observed along the border of the plastic wraps, but it is not present when $M=1.02$ or $M=3.16$, consistent with our theoretical analysis. Such an edge enhancing effect is clearly introduced by phase contrast since the thin plastic wraps contribute essentially no x-ray attenuation. In fact, the plastic wrap introduced a projected phase difference of about 2.01π between the left and right sides of the phantom when $M=1.54$, according to Equation 10.7. Though small, the phase change takes place over a very short distance at the edge, and is enough to generate intensity overshooting in the image due to Fresnel diffraction. In clinical scenarios where more substantial boundaries exist, the phase differences encountered will be much larger than that

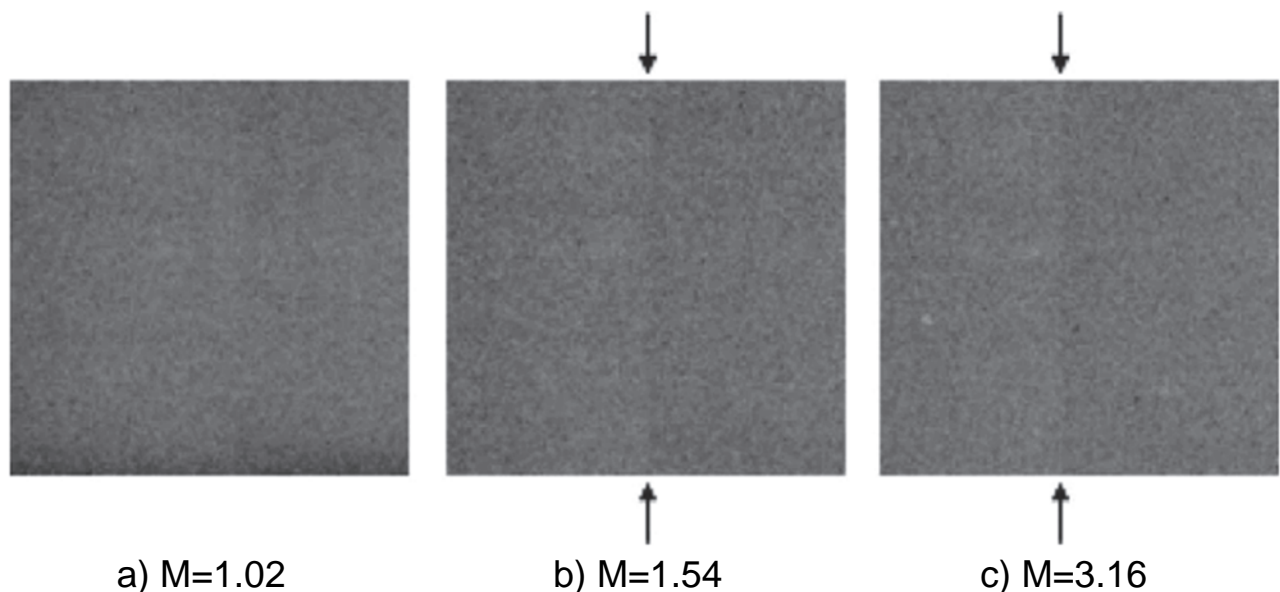


Figure 10–8. a) Phantom images acquired at $M=1.02$ show no sharp edge effect. b) Phantom images acquired at $M=1.54$ show an enhanced edge effect along the border of plastic wrap. c) At $M=3.16$, the edge effect is not as sharp as in b). (From Wu and Liu 2003b.)

created by the thin plastic wrap, and the edge enhancement is expected to be striking (Arfelli et al. 2000).

The results of these experiments agree with our theoretical analysis (Figure 10–5). In fact, the maximum phase contrast is observed at $M=1.54$, as is predicted. A further increase in M does not warrant more phase visibility, but rather causes higher breast doses. Furthermore, our experimental results validated the computer simulation results: significant phase contrast can be obtained with an in-line holography geometry at a clinically feasible source-to-detector distance (no more than 1 meter). However, it must be noted that our experiments used a thermal emission x-ray tube with an adequately small focal spot (0.02 mm), but insufficient tube current (only 0.3 mA) for the actual clinical contrast imaging of patients.

Considerations for the X-ray Tube

An x-ray tube for clinical phase-contrast mammography should have a small but bright focal spot. A small focal spot will allow adequate spatial coherence for a clinically acceptable source-to-object distance R_1 of no larger than 1 m for mammography. On the other hand, the x-ray source should have sufficient exposure rate to allow image acquisition within a few seconds. To make such a tube there are three problems to be solved (Wu and Liu 2003b).

The first difficulty is that conventional thermionic (heated filament) x-ray tubes with a microfocus cannot provide a large enough tube current for clinical use at 22 to 39 kV due to the space charge effect (Gabbay 1994). However, replacing the standard thermionic cathode with a field-emission cathode could potentially resolve this issue. Field-emission cathodes emit electrons by way of a large extraction electric field. The presence of this field at the cathode negates the buildup of a space charge cloud, ensuring that the space charge effect will not manifest unless an extremely high current density (as high as 10^9 A/cm²) is reached (Aderson 1993). Note that the current density of the proposed x-ray tube (25 mA / $(25$ μ m)²) is

several orders of magnitude smaller than this 10^9 A/cm² limit.

The second challenge is the heating of the cathode resulting from the current density of the proposed x-ray tube, which is much higher than that of conventional tubes. One potential solution is to use an electron gun made of a metallic nanocrystal material, which has been shown to operate at a current density as high as 2×10^7 A/cm² without burning out (Floreani et al. 2000). In this implementation, the field emission cathode is made of a novel material composed of nanocrystals, sized 1 to 2 nm. In each nanocrystal, the translation symmetry is completely broken and electrons become zero-dimensional (0D). The 0D material results in diminished phonon generation, since the phase-space restrictions imposed by the strong quantum confinement inhibit phonon-induced carrier relaxation (Bockelmann and Bastard 1990). On the other hand, electrons tunnel easily and quickly from excited states to neighboring crystals. The material composed from nanocrystals allows collective hopping of electrons by Coulomb interaction (Floreani et al. 2000). This leads to a non-ohmic electrical conduction with a negative temperature coefficient for the resistivity. These properties result in high field enhancement, beam confinement at the tip of the field emitter, and high currents ($>2 \times 10^7$ A/cm²) without destroying the cathode. Such a field emission source technology has been developed over the course of the past few decades, and was recently implemented in a medical imaging research system (Cao et al. 2009).

Finally, the anode must be designed to accommodate the small and bright focal spot as well. This can be achieved with only small modifications to time-honored x-ray tube technology. In fact, the increased anode heat loading can be managed by simply increasing the rotational speed and diameter of the Mo target anode or, alternatively, by employing newly intro-

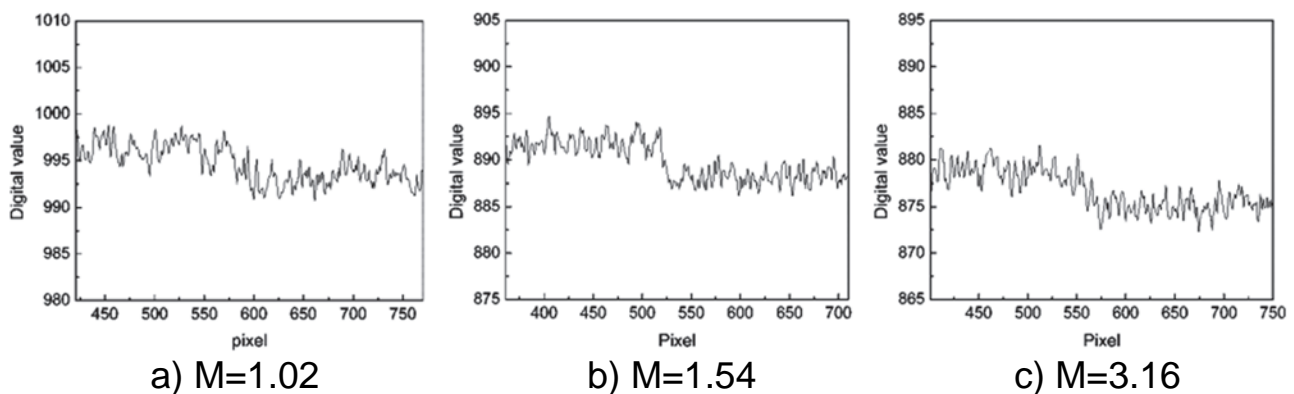


Figure 10–9. Horizontal line profiles extending across the border of plastic wrap, extracted from the images in Figure 10–8. (From Wu and Liu 2003b.)

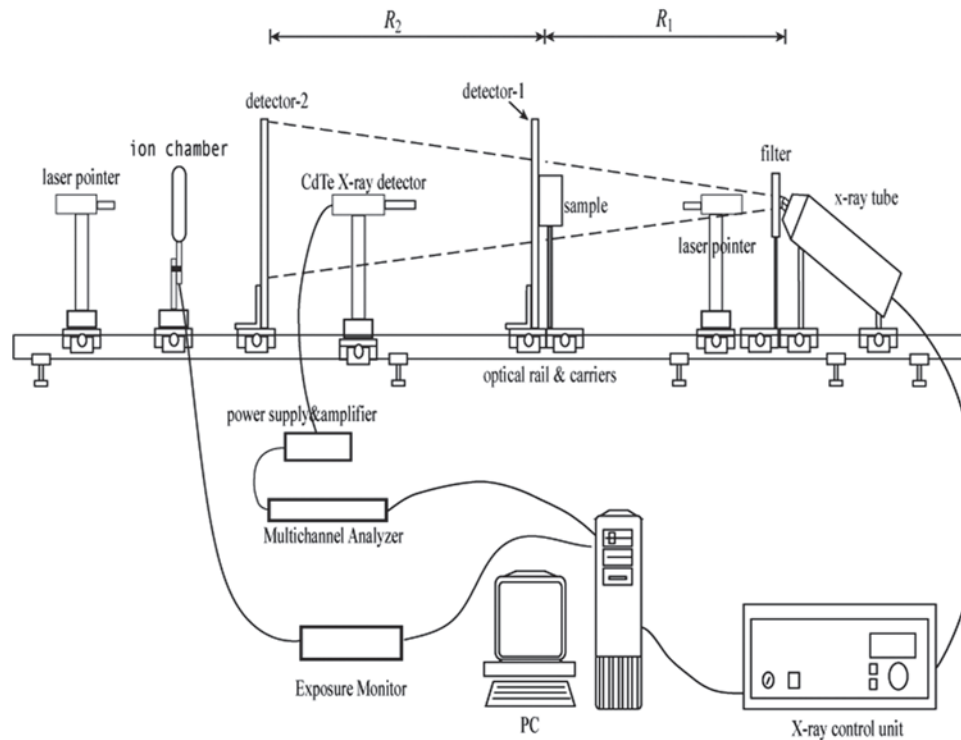


Figure 10–10. A schematic showing the dual-detector x-ray imaging system. A pure attenuation-based image is collected by detector-1, which is placed directly behind the sample. The beam reaches detector-2 after exiting detector-1, forming a phase-contrast enhanced image. Besides the core imaging components—including the x-ray source, filter, detector-1, detector-2, and the supporting optical components—the accessory systems are also shown: the ionization chamber dosimeter, the alignment laser pointers, and the CdTe-based x-ray spectrometer.

duced liquid-metal-jet-anode technology (Tuohimaa et al. 2007).

In summary, existing technologies can already provide the x-ray source characteristics necessary for phase-contrast mammography imaging, including a Mo target with a small focal spot (≤ 0.025 mm), and high tube current (≥ 25 mA). Thus, the x-ray tube challenges presented in this section already have developed solutions, and all that remains is their implementation.

10.4 Progress in System Development and the Current Status of In-line Phase-contrast Imaging

As discussed in sections 10.2 and 10.3, the physics of in-line phase-contrast imaging puts special requirements on the x-ray source, detector, and procedural details which might be outside the norm of current clinical settings. Just like the development of other new technologies, system prototyping and experimental work plays an equally important role in the overall development of in-line phase-contrast imaging technology. In this section, we report upon a few projects covering the design and development of prototype systems and their experimental validation.

10.4.1 The Design, Development, and Performance Characterization of a Dual Detector In-line Phase-contrast Imaging System

From the theories described in Section 10.2, multiple images (at least two) are needed to determine the attenuation map and the phase map from an in-line phase-contrast imaging setup. It is possible to acquire multiple images with multiple exposures using a single detector positioned at different SIDs. However, this configuration is subject to patient motion and requires high accuracy in the source–detector alignment during the detector’s downstream movement. We instead designed a dual detector approach (Wu and Liu 2004b) in which two images are obtained at different SIDs in a single exposure (Meng et al. 2007; Zhang et al. 2008).

Our prototype for in-line phase-contrast imaging consists of a micro-focus x-ray source and two specially selected digital detectors (Meng et al. 2007; Zhang et al. 2008). The detector-1 is placed in contact with the object to be imaged, while the detector-2 is placed a distance away from the object, as shown in Figure 10–10. During an x-ray exposure, only a portion of the beam is detected by detector-1, which records an attenuation-based image. The x-ray beam that exits detector-1 is then detected by the detector-2, which records a phase-con-

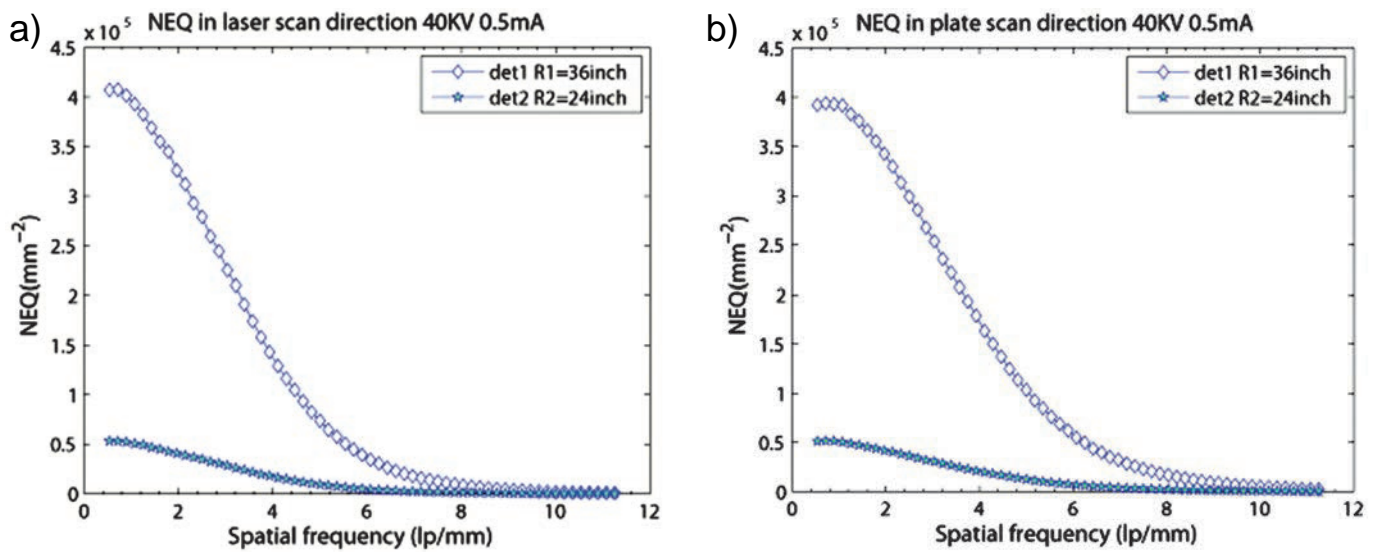


Figure 10–11. CR system NEQ curves for detector-1 and detector-2 in a) the scan (laser-scan) direction and b) the sub-scan (plate-scan) direction. The curves were obtained with a 40 kV, 0.5 mA x-ray beam, filtered by a 4 cm thick BR-12 phantom. R_1 is the distance from the source to detector-1, and R_2 is the distance between the two detectors. (From Liu et al. 2008.)

trast image. Thus, one exposure results in two images, as required for retrieving phase information, thereby eliminating the possibility of patient motion between the acquisition of the two images. One exposure also reduces the necessary x-ray exposure to the patient and concerns regarding the accuracy of detector motion.

Well-balanced x-ray exposures and quantum efficiencies for both of the detectors are critical to ensuring adequate signal-to-noise ratio (SNR) and, therefore, image quality to facilitate phase retrieval. Special attention was given to the choice

of detector-1, which must absorb an adequate number of x-ray photons in order to record the attenuation image, yet still allow enough exposure to pass through and reach the detector-2 unimpeded for its recording of the phase-contrast image. Electronic circuits and wires that exist beneath the detection layer in many digital detectors, including current flat panel technologies, would interfere with the exit fluence of the first imager, making these a poor choice for detector-1. To this end, a computed radiography (CR) plate (a photostimulable phosphor) was employed. The cassette of the phosphor was modified to replace the metal back cover with a thin carbon fiber plate to minimize unnecessary x-ray attenuation.

High quantum efficiency is the primary requirement for detector-2. In theory, several types of commercially available digital detectors could be used for the second imager, including CCD-based detector modules or flat panel detectors. For the prototype reported in this communication, a CR plate was selected for both detectors because of its adequate quantum efficiency under diagnostic energies, its sensitive response curve under relatively low photon fluence, and its ability to

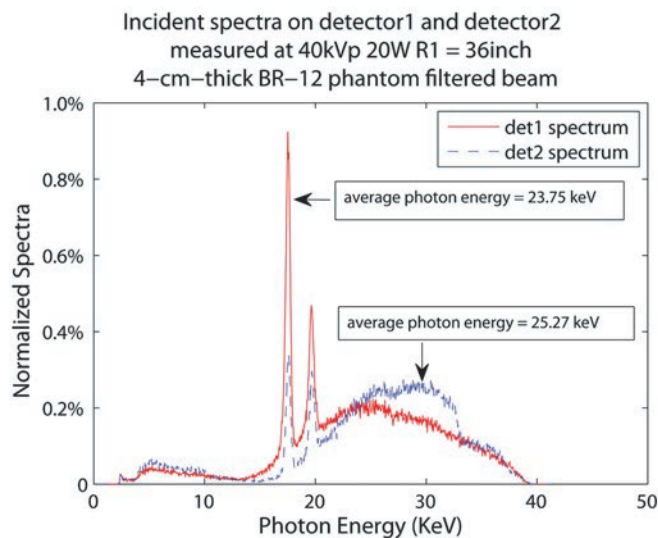


Figure 10–12. Incident spectra on detector-1 and detector-2 with a 40 kV, 0.5 mA and 4 cm thick BR-12 phantom filtered beam. Each spectrum was normalized by its total number of counts. (From Zhang et al. 2008a.)

Table 10–4: Transmittance of detector-1, measured at 40 kV with different beam filtrations
(Reprinted from Liu et al. 2008)

Beam Filtration	E1 (mR)	E1' (mR)	E2 (mR)	T (%)
No added filter	46.53	1.96	0.70	4.20
25 um rhodium	56.98	10.46	3.76	18.35
4 cm BR-12	13.58	4.42	1.59	32.54

E1 and E2 are the exposures measured at the entrance of detector-1 and detector-2, respectively. E1' is the exposure measured immediately behind detector-1. T is the transmittance of detector-1 and equals E1'/E1.

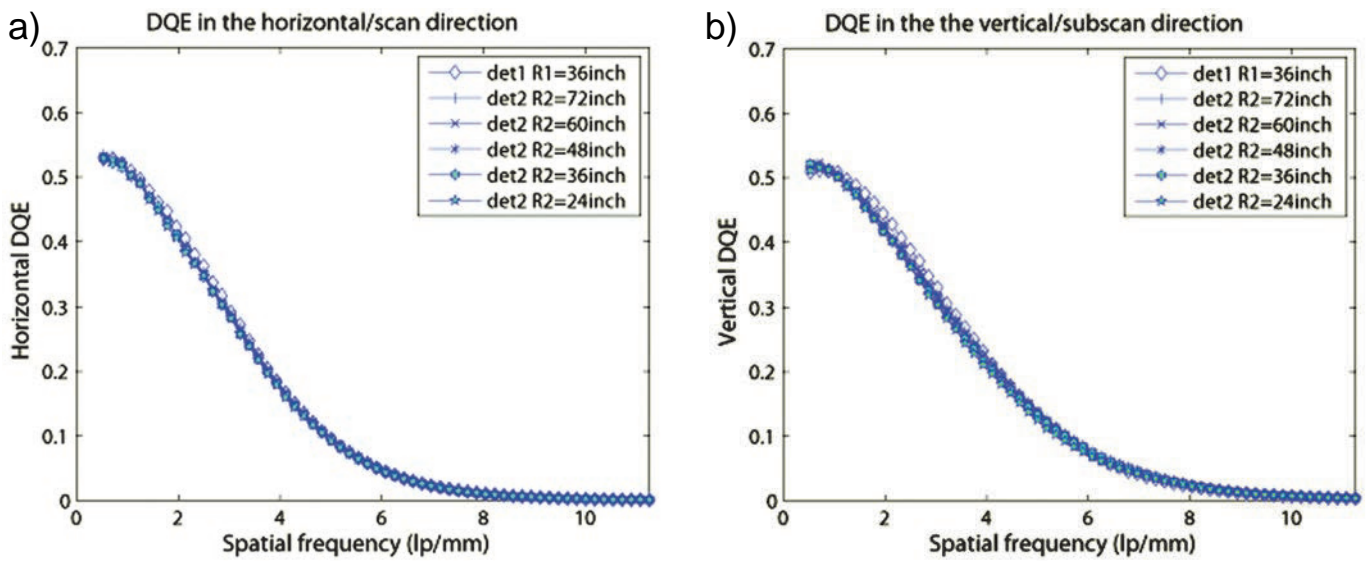


Figure 10–13. DQE in a) the scan and b) sub-scan directions for detector-1 and detector-2 at 40 kV, 12.5 mAs, $R_1=36$ in., and $R_2=24, 36, 48, 60,$ and 72 in. The beam was filtered by a 4 cm thick BR-12 phantom. (From Zhang et al. 2008a.)

allow undetected x-rays to pass through the first detector relatively unobstructed.

Experiments were conducted to characterize the detecting power and transmittance under commonly used clinical conditions. Table 10–4 summarizes the results of transmittance measurements for detector-1, acquired at 40kV with different beam filtration settings, and collected with a dosimeter system (Radcal 9095, Radcal Corp., Monrovia, CA).

To demonstrate the output SNR performance of the dual-detector imaging system, noise-equivalent quanta (NEQ)—which is defined as the square of the SNR of the recorded image (Dobbins et al. 1995; Vedantham et al. 2000)—was calculated for the prototype. The NEQ curves (Figure 10–11) were obtained for each of the detectors with a 40 kV, 0.5 mA beam filtered by 4-cm-thick BR-12 phantoms (the same imaging condition as those in row 3 of Table 10–4), based on established techniques (Dobbins et al. 1995; Vedantham et al. 2000). As illustrated, both detectors yielded NEQ values greater than 5×10^4 , but the NEQ curve of detector-1 is approximately 8 times of that of detector-2, due to the difference between the input exposure levels of the two detectors (row 3 of Table 10–4).

In the dual detector setup, the beam penetrating the first detector is also captured by the second detector. Thus the influence of the first detector on the second detector needs to be evaluated. From the NEQ and the incident exposures at the specified beam quality (Figure 10–12), the detective quantum efficiencies (DQE) (Dobbins et al. 1995; Vedantham et al. 2000) of the two detectors were estimated (Zhang et al. 2006; Zhang et al. 2008a), revealing that they are very similar in magnitude and in shape (Figure 10–13). Thus, it is apparent that the two detectors utilize x-ray quanta and transfer SNR

with similar efficiencies. The DQE values for the two detectors at very low frequencies (<0.5 lp/mm) are all above 50%, showing a highly efficient utilization of x-ray photons throughout the imaging process. The DQE curves for detector-2 with the five R_2 settings almost coincide exactly, which means that an elongated R_2 and the resultant reduced exposure levels did not degrade the imaging performance significantly under the experimental settings. The DQE curves of detector-1 also demonstrated appreciable agreement with those of detector-2, which indicates that the system performance of each detector is similar.

To illustrate the image qualities of the dual detector prototype, the wax insert of an ACR phantom was imaged with a single exposure from a 40 kV, 25 μ m thick rhodium filtered beam. Detector-1 was placed at an SID of 1.83 m and in contact with the object, and therefore recorded the attenuation-based image of the object. Detector-2 was placed 1.22 m away from detector-1, and recorded the phase-contrast image of the object. One can observe that the image from detector-2 (Figure 10–14b) is noisier than that from detector-1 (Figure 10–14a), but otherwise the overall image quality of the more distal image is not significantly degraded by the passage through the first CR plate.

To demonstrate the phase-sensitive imaging capability of the system, we developed a phase retrieval algorithm that generates a phase map from an experimentally acquired attenuation image and a phase-contrast image. The method utilized in the phase retrieval is referred to as the “attenuation-partition based phase retrieval algorithm,” which has its foundation in the general phase-contrast imaging theory described earlier (Yan et al. 2008; Yan et al. 2010; Yan et al. 2011). An illustration of the extra image information yielded by the technique

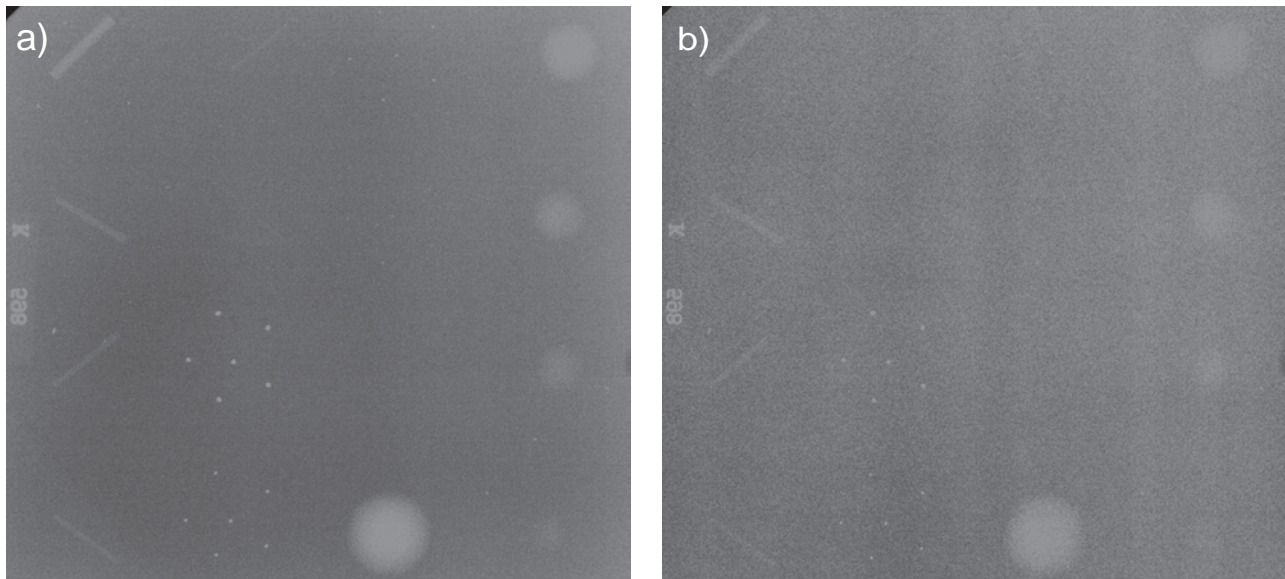


Figure 10–14. Image of a wax insert from an ACR phantom obtained by a) detector-1 and b) detector-2. These two images (attenuation and phase contrast) were acquired with a single exposure at 40 kV, 25 μm thick rhodium filtered beam.

can be obtained by imaging plastic (nylon) wraps containing many air bubbles, such as those typically used to wrap delicate objects during shipping. These plastic wraps have little attenuation due to their thickness, and thus one wouldn't expect them to be visible in a conventional x-ray image, but the abrupt refractive index change between the plastic and air bubble layers is pronounced in phase-contrast images. Figure 10–15 shows a photograph of a sample sheet of the described nylon “bubble” wrap. Figure 10–16 displays attenuation and phase-contrast images of the bubble wrap acquired individually, with a 20 μm focal spot and 40 kV beam. A phase image retrieved from the images of Figure 10–16 is presented in Figure 10–17. The color bar in this figure shows the retrieved phase values in radians. It is interesting to compare the phase-contrast image (Figure 10–16b) and the calculated phase image. While the phase-contrast image improves the visualization of the air bubbles by producing an edge enhancement effect, the final calculated phase image can be used to solve quantitatively for the object's projected electron densities for material characterization.

In addition to selecting the detection technologies, there are many other design considerations for developing an optimal phase x-ray imaging system, such as the spatial resolution of the detectors; the spatial coherence, spectrum and power of the source; and the geometry and configuration of the system, etc. Some of these were analyzed in previous publications (Wu and Liu 2003b; Wu and Liu 2004b; Wu and Liu 2007a), and others are likely topics of future investigations. Practically, the x-ray techniques, such as kV and filtration, could also be tuned according to the nature and thickness of the object to be imaged to optimally balance the stopping power

and the transmittance of the detector-1. The entirety of the phase x-ray imaging approach, including retrieval algorithms, is currently an active area of research investigation.

10.4.2 Preclinical Experiments and Subjective Evaluations

To further demonstrate the application of the in-line phase imaging system, we acquired images of a contrast detail phantom and human breast tissues (from lumpectomy) with another phase-contrast imaging prototype (Figure 10–18). Using this prototype, images of the Contrast Detail Mammography Phantom (CDMAM) phantom (Nuclear Associates, Carle Place, NY), chicken muscles (breast) and human breast tissues from a lumpectomy specimen were acquired and compared (Zhang et al. 2008b). All images were acquired with an x-ray technique setting of 40 kV, 0.25 mA, 30 s.

The same micro-focus x-ray source in the previous section was used in this prototype, but the x-ray detection system now was composed of a single direct x-ray detector made of an amorphous selenium-coated thin-film transistor (TFT) matrix (DirectRay flat panel x-ray detector, Hologic DirectRay Corporation, DE). The prototype imaging system can be configured in two modes by changing the height of the detector:

- the conventional x-ray imaging mode (hereafter referred to as conventional mode or contact mode) in which the object is positioned in contact with the detector; and
- the in-line phase contrast mode (hereafter referred to as phase contrast mode), in which the source-to-object distance (R_1), and object-to-detector distance (R_2) are both large.

In the conventional mode, the SID is 178.2 cm, while in the phase contrast mode, $R_1 = 63.5$ cm and $R_2 = 114.7$ cm, with a corresponding magnification factor $M = 2.8$. The left and middle drawings in Figure 10–19 illustrate the geometry of the system in these two experimental configurations.

Because the object is placed much closer to the source in the phase contrast mode than in the conventional mode, when the same exposure techniques are used, the absorbed dose in

the phase contrast mode is higher than that in the conventional mode by a factor of M^2 . In order to compare the performance of the phase contrast imaging techniques with conventional absorption-based imaging techniques with the same absorbed dose, we configured the system in yet another mode (hereafter referred to as the extra contact mode) in which the source-to-object distance (R_1) is still 63.5 cm, but the detector is moved closer to the source and placed in contact with the object. The

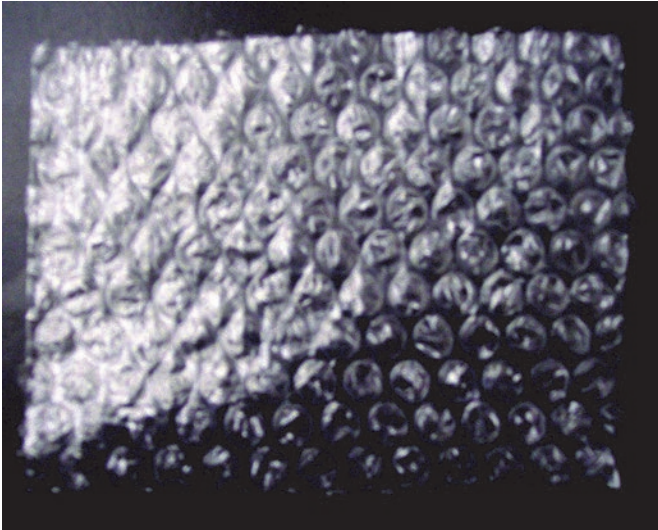


Figure 10–15. Photograph of the target used to test our phase retrieval algorithm—a nylon wrap consisting of many air bubbles.

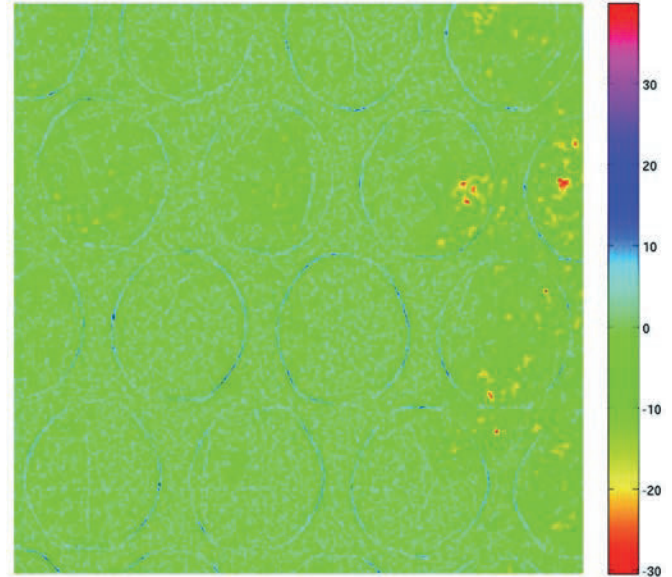


Figure 10–17. The retrieved phase map of the nylon bubble wrap based on the attenuation image (Figure 10–16a) and the phase-contrast image (Figure 10–16b). (From Liu et al. 2008.)

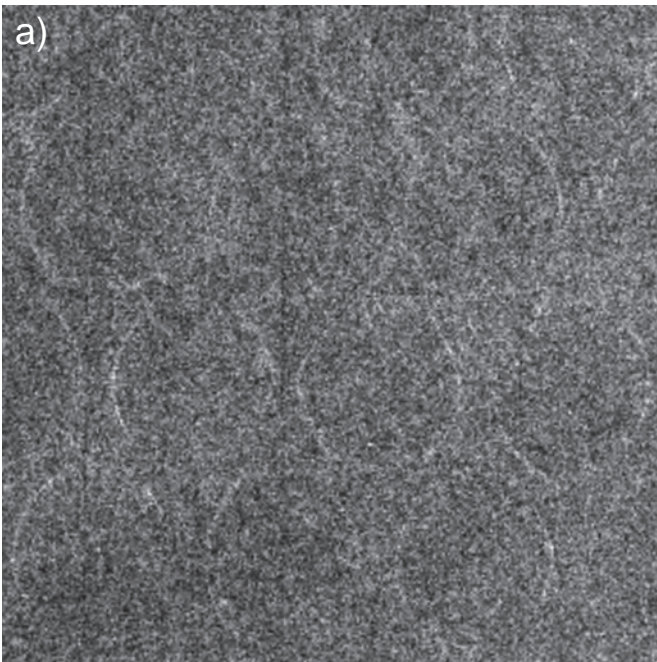


Figure 10–16. a) Attenuation image of the nylon air-bubble wrap obtained at 40 kV with SID=1.75 m; phase-contrast image. b) The same nylon wrap at $M=2.8$. (From Liu et al. 2008.)

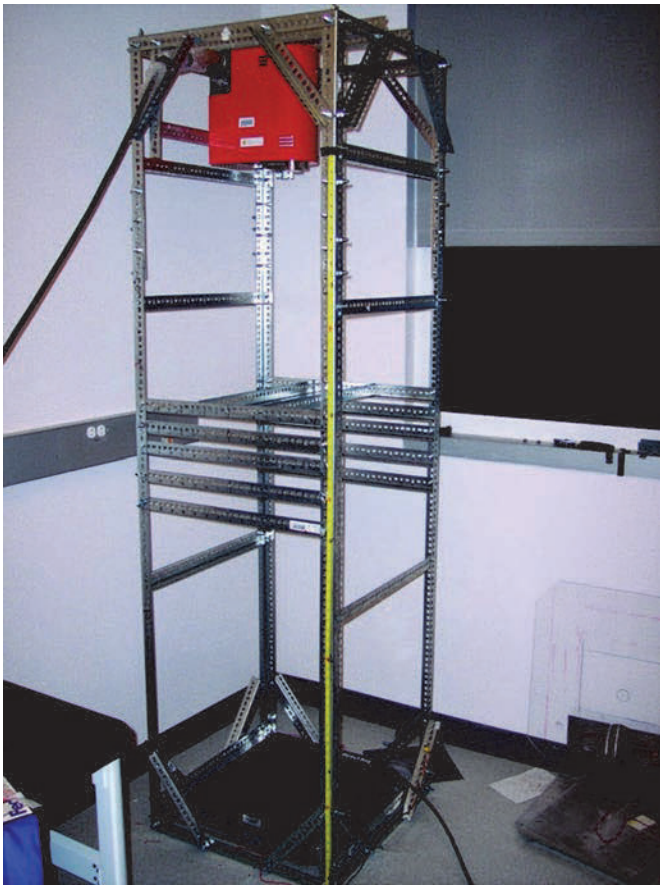


Figure 10–18. Photo of the laboratory phase-contrast imaging system used to acquire phase images of the contrast detail phantom and the human breast tissues. The SID is 178.2 cm, and the magnification factor M for the phase-contrast imaging mode is 2.8. $R_1=63.5$ cm and $R_2=114.7$ cm. For the contact mode, $R_1=R_2=SID=178.2$ cm.

drawing on the right side in Figure 10–19 illustrates the geometry of the system in this extra configuration.

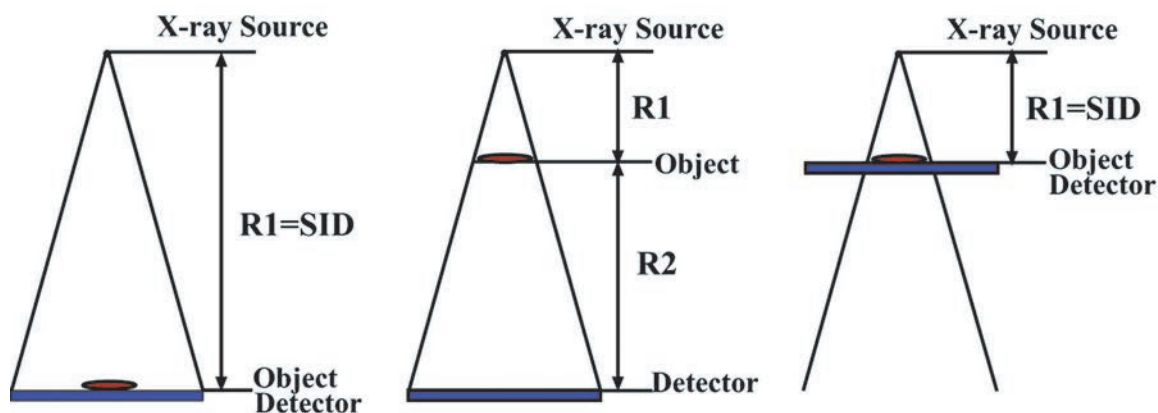


Figure 10–19. Schematic showing the geometry of the conventional imaging mode (left) and the in-line phase contrast mode (middle). The schematic on the right is also for the conventional mode, but with a reduced source-to-object distance. (From Zhang et al. 2008b).

Figure 10–20 shows images of the CDMAM phantom acquired in both conventional and phase contrast modes. Since the images of the entire CDMAM phantom are too large to be clearly presented, only a subset containing four entire squares is provided.

Figure 10–21 displays contrast-detail curves obtained for both modes, with the specified imaging technique. All curves represent the average results from 11 human observers; the error bars in the figures indicate the 95% confidence interval for each data point, based upon a student’s t -distribution with a degree of freedom of 10. For the purpose of comparing the phase contrast technique with the conventional technique under the condition of the same absorbed dose, Figure 10–22 shows the contrast-detail curve obtained in both the phase contrast mode and the “extra contact mode,” both performed with a source to object distance of 63.5 cm.

The contrast-detail curves display a measurement of the threshold contrast (represented by the minimum perceptible disk thickness) needed to detect an object as a function of its diameter (Darambara et al. 2000), and provide us with an effective method for comparing the performance of the conventional x-ray imaging technique with the phase contrast imaging technique. The curves representing the conventional mode start at a diameter equal to 0.13 mm, which represents the limiting resolution of the system in conventional mode. On the other hand, the curves of the phase contrast mode start at a diameter equal to 0.1 mm with a relatively low threshold contrast, which is probably because the effective resolution ($139/2.8 \approx 49.6 \mu\text{m}$) of the system in the phase contrast mode with a magnification factor 2.8 is much higher than the limiting resolution measurable by the CDMAM phantom (100 μm). From figures 10–21 and 10–22, one can see that with the same disk diameter, the phase contrast imaging mode requires lower contrast for the disks to be visible than the conventional mode, and therefore exhibits higher performance. Although

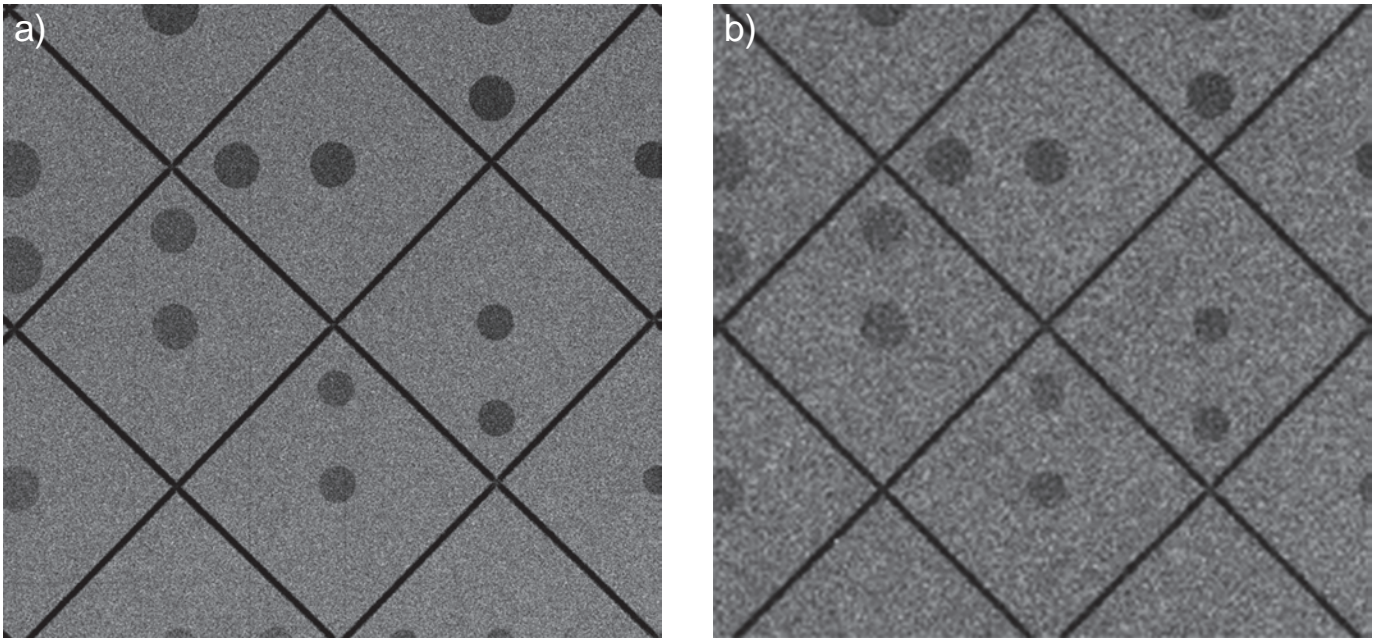


Figure 10–20. Region of interest from the CDMAM phantom in a) phase contrast mode and b) conventional mode. (From Zhang et al. 2008b.)

the two curves in Figure 10–22 are much closer to each other, one can still observe that the contrast-detail curve of the phase contrast at lower diameters is lower than that of the “extra contact mode,” which means the former still requires lower

contrast for disks with small diameter than the latter. The reason why the contrast-detail curve of the extra contact mode is better behaved than that of the conventional mode is that the exposure on the detector entrance in the former case is about

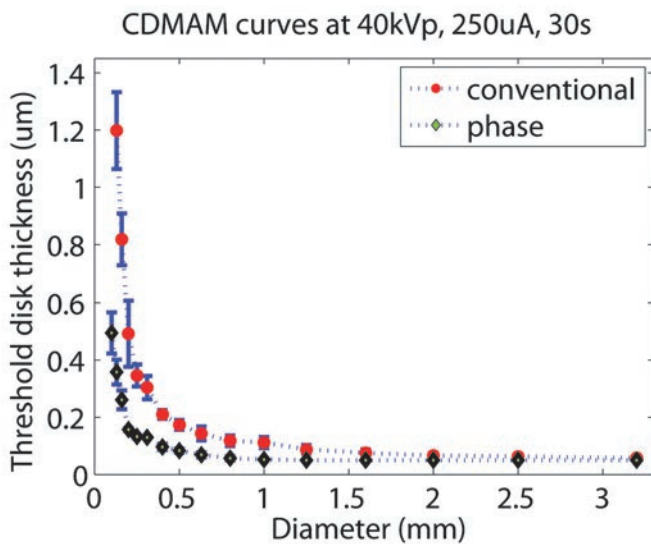


Figure 10–21. Comparison of the average contrast-detail curves generated by 11 human observers viewing conventional and phase-contrast images. In the conventional mode, the SID is 178.2 cm, while in the phase contrast mode, $R_1=63.5$ cm and $R_2=114.7$ cm. The error bars indicate the 95% confidence interval for each data point based on a student’s t-distribution. (From Zhang et al. 2008b.)

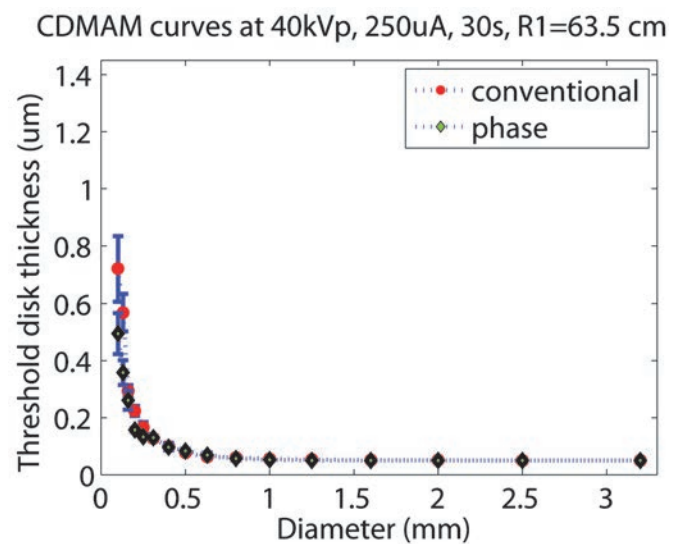


Figure 10–22. Comparison of the average contrast-detail curves generated by 11 human observers viewing conventional and phase-contrast images of a CDMAM phantom. Both images were taken with the same source-to-object distance ($R_1=63.5$ cm) and, hence, the same absorbed dose. The error bars indicate the 95% confidence interval for each data point based on a student’s t-distribution. (From Zhang et al. 2008b.)

7.84 times higher than in the latter, resulting in a 2.8 times higher SNR in the former than in the latter, and therefore much better image quality.

In Figure 10–23, a chicken breast specimen (unfixed tissues of 1 mm thickness) was imaged in both conventional and phase contrast modes with the previously described x-ray settings. Figure 10–24 shows images of a different chicken breast specimen with artificial calcifications (pieces of chewable calcium placed on top of the tissue) which together simulate a core biopsy sample. It is evident that the structures are more clearly defined in the phase-contrast images than in the conventional images. In particular, edge enhancement resulting from the in-line phase contrast approach results in bright and dark fringes along the boundaries of the tissues and bubbles in both figures, and the calcifications appear enhanced in the phase-contrast image of Figure 10–24.

Figure 10–25 shows the x-ray images of a human lumpectomy specimen containing a lesion, whose position is indicated by an inserted needle. Similar to the chicken tissue images, the dark–bright fringes along the boundaries of the tissue and air bubbles can be clearly seen. In addition, the

retrieved phase image of the lumpectomy specimen, acquired with the “attenuation-partition based phase retrieval algorithm” (Yan et al. 2008; Yan et al. 2010; Yan et al. 2011) is displayed. This phase map shows the projected phase values in unit of radians. Projected electron densities obtained from this phase map (not shown in the figure) agreed with the thickness profile of the specimen. Figure 10–26 displays more closely the region of the lesion, which allows the edge enhancement on the boundaries of the lesion tissue and air bubbles to be more notably observed. Figure 10–27 presents images of three core biopsy specimens from a different human subject, yielding still further evidence of the improved clarification of boundaries provided by the phase imaging approach.

Considering the low spatial resolution of the detector (139 μm), the relatively low detector entrance exposure (37.3 mR) and comparatively high tube potentials (40 kV), such findings are encouraging to the future of phase contrast research. Along with edge enhancement, images obtained in the phase contrast mode exhibit better overall image quality than those obtained in the conventional mode. However, it should be noted that this overall improvement in image qual-

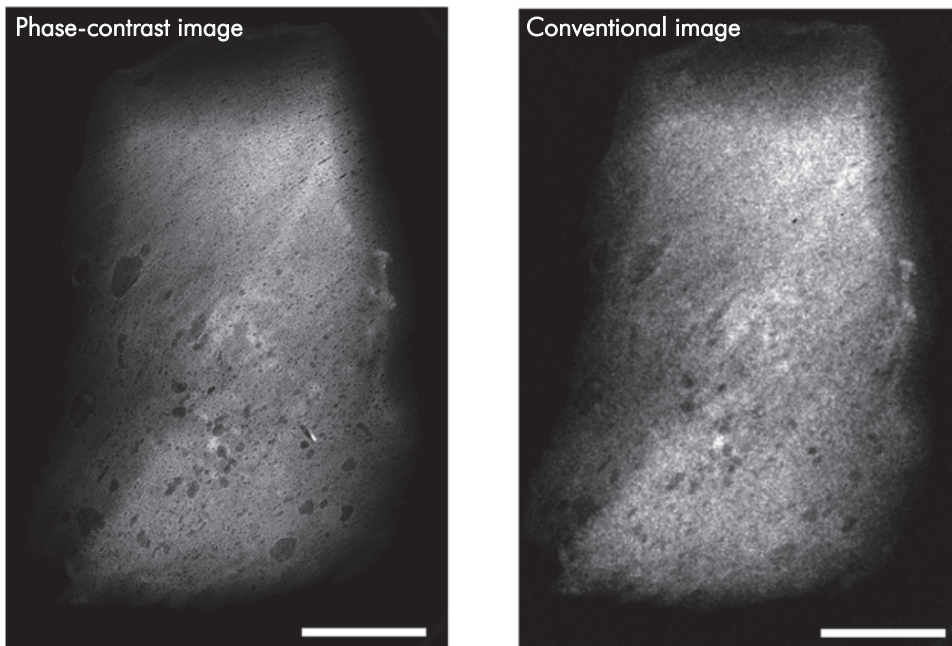


Figure 10–23. Comparison between phase contrast and conventional x-ray images of 1 mm thick chicken breast tissue. The scale bar in each image represents a length of 1 cm. (From Zhang et al. 2008b.)

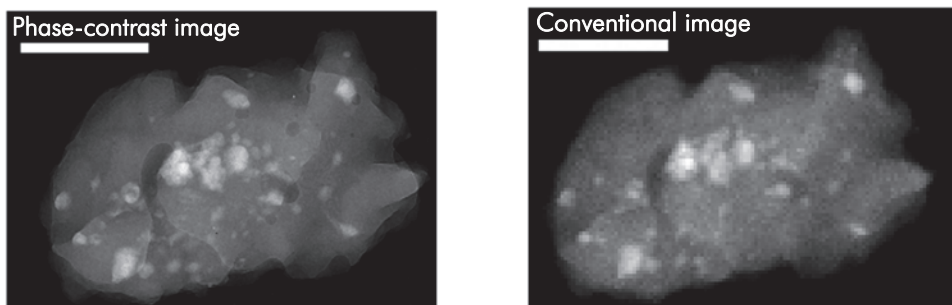


Figure 10–24. Comparison between phase contrast and conventional x-ray images of chicken breast tissue with artificial calcifications simulating a human breast core biopsy specimen. The scale bar in each image represents a length of 5 mm. (From Zhang et al. 2008b.)

ity is a result of both the phase effect and the magnification, which leads to higher effective spatial resolution. A future goal for phase contrast research is to utilize a higher-energy x-ray beam, which holds the potential to reduce the absorbed dose without negatively affecting the image quality due to the fact that the phase-contrast imaging technique does not rely solely upon attenuation for image formation. A brighter x-ray source with a micro focal spot is also desirable, as these sample images were acquired with long exposure times of 30 s, which would not be ideal in a clinical setting. Finally, further studies are necessary to investigate the impact of improved edge detectability on diagnostic measures, as it is possible that these pronounced features may confuse image interpreta-

tion on the part of the radiologist, in addition to improving feature visibility.

10.4.3 Phase Duality-based Robust Phase Retrieval from a Single Phase-contrast Image

Phase retrieval is an important step in phase-sensitive imaging to quantify phase changes caused by tissues (Wu and Liu 2003a; Wu and Liu 2004c; Wu and Liu 2005). The in-line holography principle requires that, in general, at least two images are needed for phase retrieval. One can acquire the multiple images either by using multiple x-ray exposures or by employing multiple detectors with a single exposure, as discussed in the previous sections.

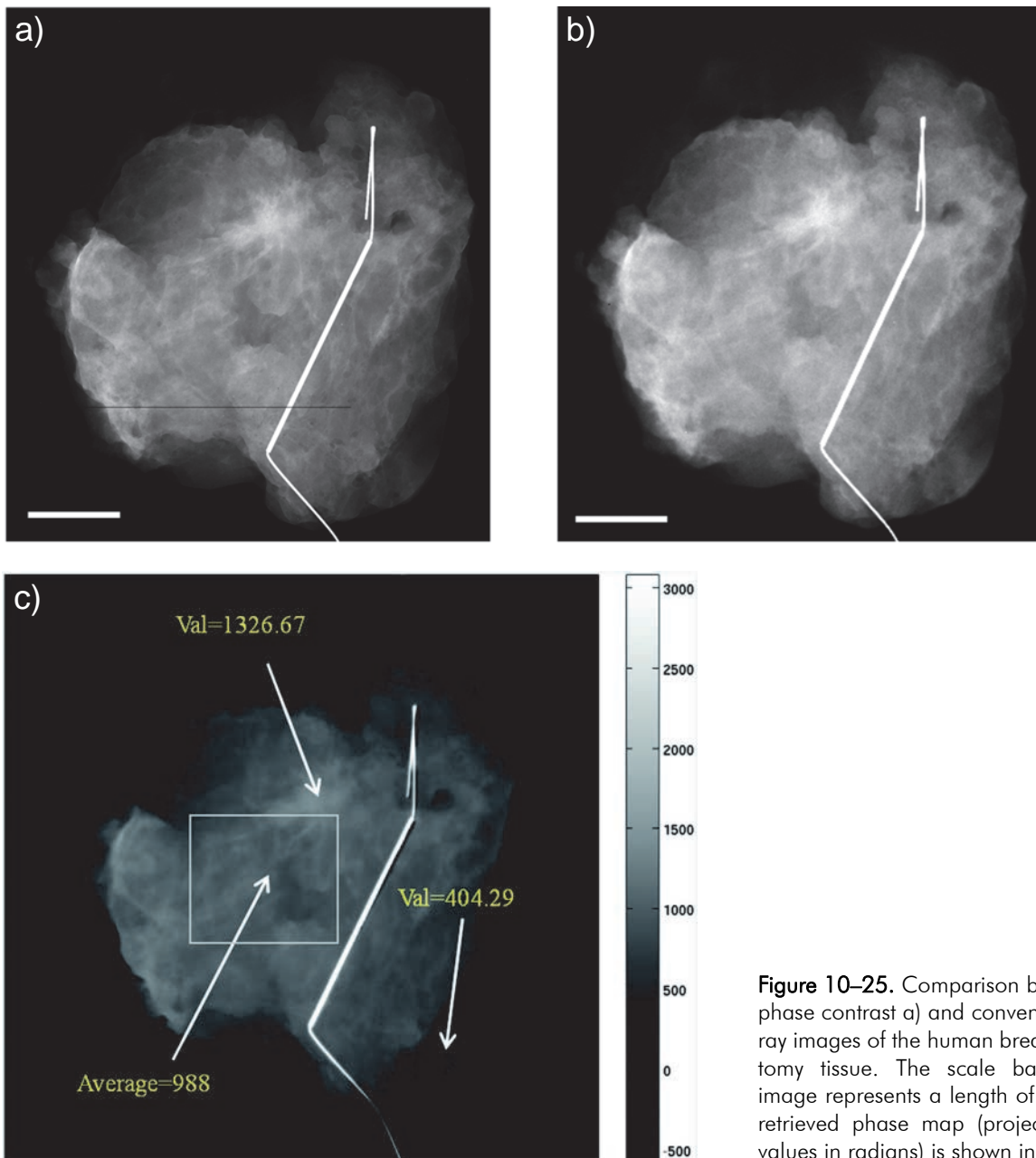


Figure 10–25. Comparison between the phase contrast a) and conventional b) x-ray images of the human breast lumpectomy tissue. The scale bar in each image represents a length of 1 cm. The retrieved phase map (projected phase values in radians) is shown in c).

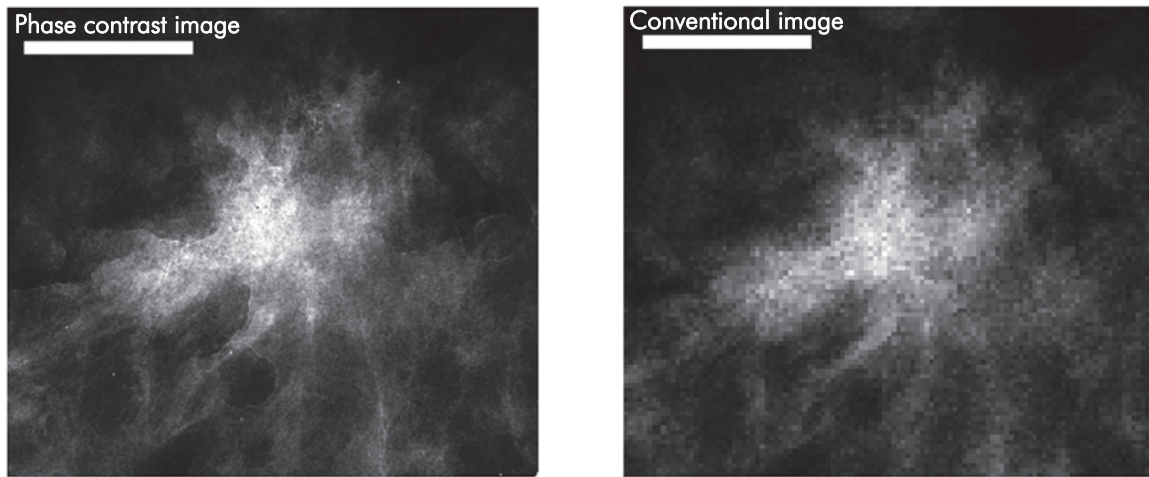


Figure 10–26. Lesion area of the lumpectomy tissue demonstrates the edge enhancement provided by phase-contrast imaging. The scale bar in each image represents a length of 5 mm. (From Zhang et al. 2008b.)

This requirement for multiple image acquisitions adds some complexity to clinical implementation of phase imaging, because in clinical imaging the motion artifacts and the radiation dose should be stringently controlled (Wu and Liu 2003b; Wu and Liu 2004b). The complexity of multiple image acquisition also adds difficulty to the implementation of x-ray phase CT (Wu and Liu 2004a). In this section we first present phase-attenuation duality for soft tissues (Wu et al. 2005; Wu and Liu 2007b), and show that the high sensitivity of phase imaging manifests itself from the high ratio of x-ray wavelength to classic electron radius in the presence of the phase-attenuation duality. Utilizing this duality, we derive a phase-retrieval formula based on only a single phase-contrast image acquired with a point x-ray source.

For phase-contrast imaging an object can be modeled as a 2D transmission function in the object plane perpendicular to the direction of x-ray projection with its amplitude denoted by $A(\mathbf{r})$ and its phase by $\phi(\mathbf{r})$. The map $A^2(\mathbf{r})$ is the tissue's x-ray attenuation image, and the map $\phi(\mathbf{r})$ is the tissue's x-ray phase image. While the tissue phase arises from x-ray coherent scat-

tering, the tissue attenuation arises from three x-ray–tissue interactions: photoelectric absorption, coherent scattering, and incoherent scattering for the x-rays employed in clinical imaging (Wu et al. 2005).

Soft tissues encountered in clinical imaging are mainly composed of light elements with atomic numbers $Z < 10$. For example, breast tissue comprises light elements such as hydrogen, carbon, nitrogen, and oxygen. On the other hand, the sum weight of all the other, heavier elements in breast tissue is only 1.4% (ICRU 1989). The same is true for other soft tissues, such as gray-white brain matter (Wu et al. 2005).

It can be shown by analyzing the existing tissue attenuation data that for x-rays of approximately 60 to 500 keV, the soft tissue attenuation cross sections are approximated by those of x-ray incoherent scatter with small errors from 10% to 0.16%, and the incoherent scattering function becomes linearized as well such that incoherent scattering is proportional to atomic number of the element (Dyson 1973; Wu et al. 2005). Under this situation we find that $A(\mathbf{r})$ depends on the tissue electron density $\rho_{e,p}(\mathbf{r},z)$ as (Wu et al. 2005; Wu and Liu 2007b):

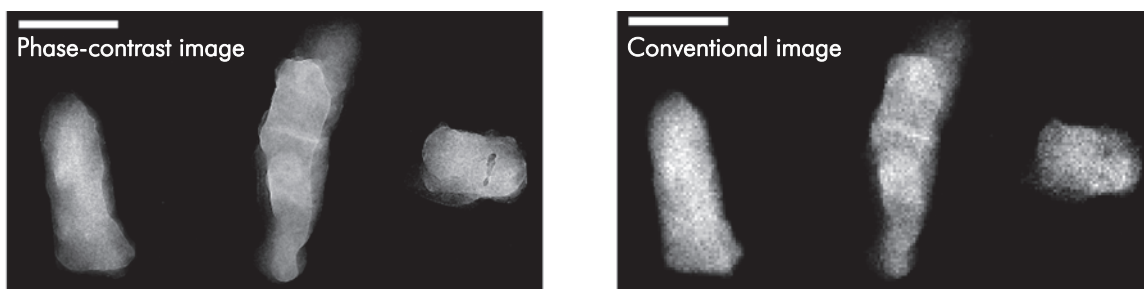


Figure 10–27. Detailed images of a human core biopsy specimen. The scale bar in each image represents a length of 5 mm. (From Zhang et al. 2008b.)

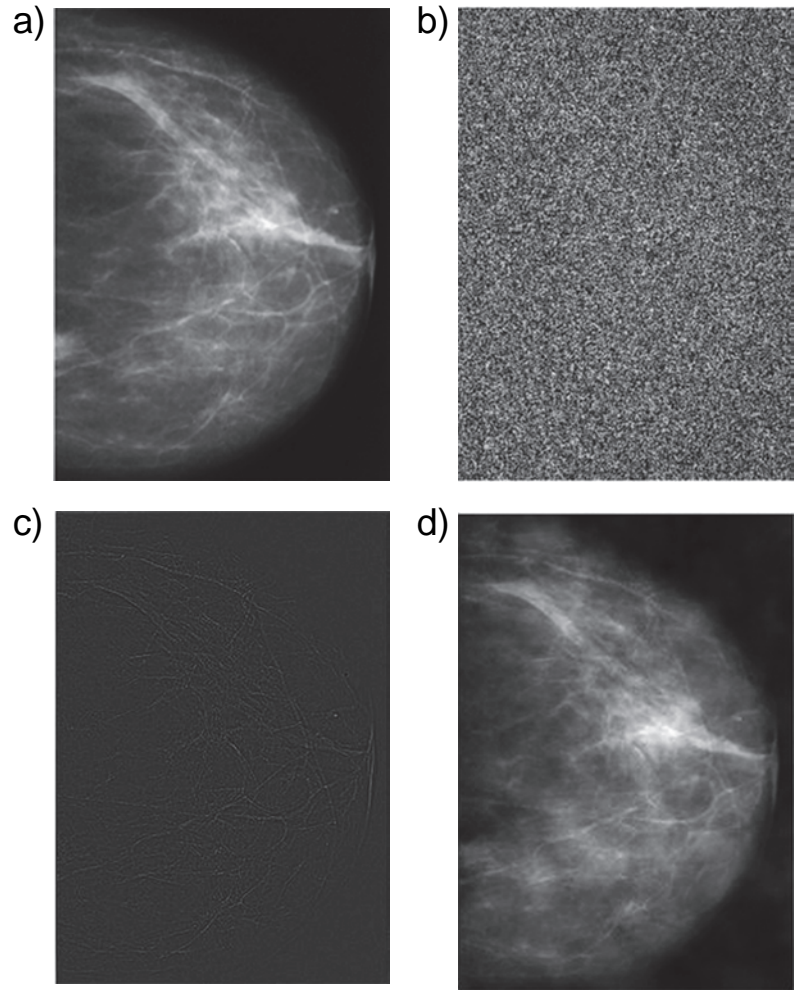


Figure 10–28. a) Simulated image of projected electron density for a hypothetical breast of 4 cm thickness with very low tissue radiographic subject contrast, $\leq 0.83\%$ for 60 keV x-rays. b) Simulated attenuation image with added random noise of 5% of $A^2(\mathbf{r})$. The image is entirely masked by the small added noise. c) Simulated phase-contrast image with 5% random noise. The edges between tissue components are greatly enhanced, but bulk tissue contrast within any given tissue compartment is lost. d) Retrieved phase image of the hypothetical breast from the noisy phase-contrast image using the phase-attenuation duality approach. (From Wu and Liu 2007b.)

$$\begin{aligned}
 A(\mathbf{r}) &\approx \exp\left[-\frac{\sigma_{KN}}{2} \int \rho_e(\mathbf{r}, z) dz\right] \\
 &= \exp\left[-\frac{\sigma_{KN}}{2} \rho_{e,p}(\mathbf{r})\right]
 \end{aligned}
 \quad (10.41)$$

where the projected electron density $\rho_{e,p}(\mathbf{r})$ is the integral of the electron density over the ray path. Here σ_{KN} is the total cross section for x-ray photon Compton scattering from a single free electron, derived from the Klein–Nishina formula:

$$\begin{aligned}
 \sigma_{KN} = 2\pi r_e^2 \left\{ \frac{1+\eta}{\eta^2} \left[\frac{2(1+\eta)}{1+2\eta} - \frac{1}{\eta} \log(1+2\eta) \right] \right. \\
 \left. + \frac{1}{2\eta} \log(1+2\eta) - \frac{1+3\eta}{(1+2\eta)^2} \right\}.
 \end{aligned}
 \quad (10.42)$$

In Equation 10.42, $\eta = E_{photon}/m_e c^2$, where E_{photon} is the photon energy of the primary x-ray beam, is the resting electron energy and is equal to 511 keV, and r_e is the classic electron radius. If the x-ray energy is away from the absorption

edge of the tissue, we can write the tissue phase $\phi(\mathbf{r})$ as (Poganiin et al. 1997; Wu et al. 2005; Wu and Liu 2007b):

$$\phi(\mathbf{r}) = -\lambda r_e \int \rho_e(\mathbf{r}, z) dz = -\lambda r_e \rho_{e,p}(\mathbf{r}) \quad (10.43)$$

where λ is the x-ray wavelength. Comparing Equations 10.41 and 10.43, we can make an important observation: both the phase image $\phi(\mathbf{r})$ and the attenuation image $A^2(\mathbf{r})$ of soft tissue are determined by the same map of projected electron density, $\rho_{e,p}(\mathbf{r})$, assuming that the x-ray photon energies are in the approximate range of 50 to 600 keV. We call this complementary relationship between phase and attenuation for soft tissues the phase-attenuation duality, considering the different origins of x-ray soft tissue interactions for phase and attenuation, respectively (Wu et al. 2005).

Based on the phase-attenuation duality for soft tissues, we derived a new phase-retrieval formula from a single phase-contrast image acquired with a point source. As described previously, let the distance from a monochromatic point source to the object plane be R_1 and the distance from the object plane to the detector plane be R_2 ; hence, geometric

magnification factor $M = (R_1 + R_2) / R_1$. Starting from either the paraxial Fresnel–Kirchhoff diffraction theory or the phase-space evolution of the Wigner distributions for x-ray wave fields, after a tedious calculation we found the following formula for $\rho_{e,p}(\mathbf{r})$ (Wu et al. 2005; Wu and Liu 2007b):

$$\rho_{e,p}(\mathbf{r}) = -\frac{1}{\sigma_{KN}} \times \log_e \left(FT^{-1} \left[\frac{FT[M^2 I(M\mathbf{r}; R_1 + R_2)}{I_{in} \left[1 + 2\pi \frac{\lambda^2 r_e R_2}{M \sigma_{KN}} \mathbf{u}^2 \right]} \right] \right), \quad (10.44)$$

where $I(M\mathbf{r}; R_1 + R_2)$ is the image intensity at the detector plane and I_{in} is the intensity at the subject entrance. FT and FT^{-1} denotes the 2D Fourier transform and its inverse, and \mathbf{u} is the spatial frequency vector in the object plane. Note that the retrieved image $\rho_{e,p}(\mathbf{r})$ of the projected electron density represents both the phase image and the attenuation image by equations 10.41 and 10.43.

Here we want to point out that the high sensitivity of the x-ray phase change is obtained as the large ratio $\lambda r_e / \sigma_{KN} \gg 1$ in this circumstance. In fact, for clinical imaging the photon energy is typically no higher than 150 keV, and in this case $\lambda r_e / \sigma_{KN} \approx 3\lambda / 8\pi r_e \sim 10^4$. With this duality, the high sensitivity of the phase imaging manifests itself from a large ratio of x-ray wavelength to classic electron radius.

To demonstrate the application of the phase-attenuation duality in phase retrieval, we simulated the in-line phase contrast imaging of a hypothetical breast (Wu et al. 2005; Wu and Liu 2007b). The simulation was conducted with $R_1 = R_2 = 1$ m, a point source, and a perfect detector. The object-pixel size was 2 μm in a 512-by-512 matrix. The hypothetical breast was 4 cm thick with subject contrast $\leq 0.83\%$ for a 60 keV x-ray.

The original projected electron density map of the breast is shown in Figure 10–28a. Figure 10–28b displays the simulated attenuation image with 5% added random noise in $A^2(\mathbf{r})$, enough to completely mask the tissue contrast (Wu and Liu 2007b). Figure 10–28c demonstrates the Fresnel diffraction-simulated phase-contrast image containing the 5% added random noise. Note that the edges between different tissue components are greatly enhanced in this image, but bulk tissue contrast within any given tissue compartment is lost. We applied Equation 10.44 to the phase-contrast image for phase retrieval. Figure 10–28d shows the retrieved phase image of the breast in Figure 10–28a with an average relative phase-error of 0.11%. The “true” tissue contrast is restored in this phase image of the simulated breast. Compared to the attenuation-based image of Figure 10–28b, the retrieved phase image demonstrates striking noise suppression.

The relative phase-error of 0.11% demonstrates that this new phase retrieval method is robust, which is critically important for diagnostic imaging, especially in light of dose considerations. Our calculations show that pathological changes in the breast may be associated with very small phase changes. For example, because the difference in phase-shift between a 2.5 mm invasive ductal carcinoma and normal breast parenchyma is only a few radians, a small phase-error is crucial. The high sensitivity and robust nature of this phase imaging method suggests that it has great potential to enhance the sensitivity of lesion detection while reducing the radiation dose associated with clinical imaging.

10.5 Summary

In-line phase x-ray imaging shows remarkable potential as a diagnostic imaging tool. The major factor that limits the clinical adoption of the modality is still related to the x-ray source. Currently, commercially available micro-focus x-ray tubes require extended exposure times due to low photon flux and large SID geometries. However, we anticipate that the ongoing technical development of new x-ray sources will successfully boost the translation of this important imaging technology from the research laboratory to the clinic.

10.6 Acknowledgment

The authors would like to thank Dr. Laurie L. Fajardo of the University of Iowa for her collaborations in phase-sensitive x-ray imaging research. Additionally, some of the clinical images presented in this chapter were acquired in her clinical facility.

10.7 References

- Aderson, W. (1993). “Role of Space Charge in Field Emission Cathodes.” *J. Vac. Sci. Technol.* B11:383–386.
- Arfelli, F., Valter Bonvicini, A. Bravin, G. Cantatore, E. Castelli, L. Dalla Palma, M. Di Michiel, M. Fabrizioli, R. Longo, R. H. Menk, A. Olivo, S. Pani, D. Pontoni, P. Poropat, M. Prest, A. Rashevsky, M. Ratti, L. Rigon, G. Tromba, A. Vacchi, E. Vallazza, and F. Zanconati. (2000). “Mammography with Synchrotron Radiation: Phase Detected Techniques.” *Radiology* 215:286–293.
- Bockelmann, U. and G. Bastard. (1990). “Phonon Scattering and Energy Relaxation in Two-, One-, and Zero-dimensional Electron Gases.” *Phys. Rev. B. Condens. Matter.* 42:8947–8951.
- Born, M. and E. Wolf. *Principles of Optics*, 6th ed. Oxford: Pergamon Press Ltd., 1980.
- Cao, G., Y. Z. Lee, R. Peng, Z. Liu, R. Rajaram, X. Calderón-Colon, L. An, P. Wang, T. Phan, S. Sultana, D. S. Lalush, J. P. Lu, and O. Zhou. (2009). “A Dynamic Micro-CT Scanner Based on a Carbon Nanotube Field Emission X-ray Source.” *Phys. Med. Biol.* 54(8):2323–2340.
- Chapman, D., W. Thomlinson, R. E. Johnston, D. Washburn, E. Pisano, N. Gmür, Z. Zhong, R. Menk, F. Arfelli, and D. Sayers. (1997). “Diffraction Enhanced X-ray Imaging.” *Phys. Med. Biol.* 42:2015–2025.
- Darambara, D.G., A. Taibi, R. D. Speller, and M. Gambaccini. (2000). “Contrast Detail Evaluation of a Full-field Digital Mammography System.” *IEEE Trans. Nucl. Sci.* 47(3):870–876.
- Dobbins, J. T., D. L. Ergun, L. Rutz, D. A. Hinshaw, H. Blume, and D. C. Clark. (1995). “DQE(f) of 4 Generations of Computed Radiography Acquisition Devices.” *Med. Phys.* 22(10):1581–1593.

- Dyson, N. *X-rays in Atomic and Nuclear Physics*. London: Longman Group Limited, 1973.
- Floreani, F., H. Koops, and W. Elsaesser. (2000). "Operation of High Power Field Emitters Fabricated with Electron Beam Induced Deposition." EuroFE2000 Scientific Program, September 25–29, 2000, Segovia, Spain.
- Gabbay, E. "X-ray Source Assembly Design" in *Specification, Acceptance Testing and Quality Control of Diagnostic X-ray Imaging Equipment*. Medical Physics Monograph No. 20, J. Seibert, G. Barnes, and R. Gould, eds. Woodbury, NY: American Institute of Physics, 1994.
- Goodman, J. W. *Statistical Optics*. New York: John Wiley & Sons, Inc., 2000.
- Hubbel, J. H. (1982). "Photon Mass Attenuation and Energy-absorption Coefficients from 1keV to 20 MeV." *Int. J. Appl. Radiat. Isot.* 33:1269–1290.
- ICRU. International Commission on Radiation Units and Measurements. ICRU Report 44. *Tissue Substitutes in Radiation Dosimetry and Measurement*. Bethesda, MD: ICRU, 1989.
- Littlejohn, R. G. (1986). "The Semiclassical Evolution of Wave Packets." *Phys. Rep.* 138(4–5):193–291.
- Liu, H., D. Zhang, X. Wu. (2008). "Development of a Dual Detector Phase X-ray Imaging System: Design Considerations." Proceeding of the IEEE Southwest Symposium on Image Analysis and Interpretation (SSIAI 2008):193–196.
- Mandel, L. and E. Wolf. *Optical Coherence and Quantum Optics*. Cambridge: Cambridge University Press, 1995.
- Meng, F., A. Yan, G. Zhou, X. Wu, and H. Liu. (2007). "Development of a Dual-detector X-ray Imaging System for Phase Retrieval Study." *Nuclear Instruments and Methods in Physics Research B* 254:300–306.
- Momose, A. (2003). "Phase-sensitive Imaging and Phase Tomography Using X-ray Interferometers." *Opt. Express* 11:2303–2314.
- Momose, A. and J. Fukuda. (1995). "Phase-contrast Radiograph of Non-stained Rat Cerebellar Specimen." *Med. Phys.* 22:375–379.
- Quandji, F., E. Potter, W. R. Chen, Y. Li, D. Tang, and H. Liu. (2002). "Characterization of a CCD-based Digital X-ray Imaging System for Small-animal Studies: Properties of Spatial Resolution." *Appl. Opt.* 41(13):2420–2427.
- Piestrup, M. A., X. Wu, V. V. Kaplan, S. R. Uglov, J. T. Cremer, D. W. Rule, and R. B. Fiorito. (2001). "A Design of Mammography Units Using a Quasimonochromatic X-ray Source." *Rev. Sci. Instrum.* 27:2159–2170.
- Pogany, A., D. Gao, and S.W. Wilkins. (1997). "Contrast and Resolution in Imaging with a Microfocus X-ray Source." *Rev. Sci. Instrum.* 68(7):2774–2782.
- Tucker, D. M., G. T. Barnes, and X. Wu. (1991). "Molybdenum Target X-ray Spectra: A Semiempirical Model." *Med. Phys.* 18:402–407.
- Tuohimaa, T., M. Otendal, and H. M. Hertz. (2007). "Phase-contrast X-ray Imaging with a Liquid-metal-jet-anode Microfocus Source." *Appl. Phys. Lett.* 91(7):074104–074104–3.
- Vedantham, S., A. Karellas, S. Suryanarayanan, D. Albagli, S. Han, E. J. Tkaczyk, C. E. Landberg, B. Opsahl-Ong, P. R. Granfors, I. Levis, C. J. D'Orsi, and R. E. Hendrick. (2000). "Full Breast Digital Mammography with an Amorphous Silicon-based Flat Panel Detector: Physical Characteristics of a Clinical Prototype." *Med. Phys.* 27:558–567.
- Weitkamp, T., A. Diaz, C. David, F. Pfeiffer, M. Stampanoni, P. Cloetens, and E. Ziegler. (2005). "X-ray Phase Imaging with a Grating Interferometer." *Optics Express* 13(16):6296–6304.
- Wilkins, S. W., T. E. Gureyev, D. Gao, A. Pogany, and A. W. Stevenson. (1996). "Phase-contrast Imaging Using Polychromatic Hard X-rays." *Nature* 384:335–338.
- Wu, X. and H. Liu. (2003a). "A General Theoretical Formalism for X-ray Phase Contrast Imaging." *J. X-ray Sci. Tech.* 11(1):33–42.
- Wu, X. and H. Liu. (2003b). "Clinical Implementation of X-ray Phase-contrast Imaging: Theoretical Foundations and Design Considerations." *Med. Phys.* 30(8):2169–2179.
- Wu, X. and H. Liu. (2004a). "A Reconstruction Formula for Soft Tissue X-ray Phase Tomography." *J. X-ray Sci. Tech.* 12(4):273–279.
- Wu, X. and H. Liu. (2004b). "A Dual Detector Approach for X-ray Attenuation and Phase Imaging." *J. X-ray Sci. Tech.* 12(1):35–42.
- Wu, X. and H. Liu. (2004c). "A New Theory of Phase-contrast X-ray Imaging Based on Wigner Distributions." *Med. Phys.* 31(9):2378–2384.
- Wu, X. and H. Liu. (2005). "Phase-space Formulation for Phase Contrast X-ray Imaging." *Appl. Opt.* 44(28):5847–5854.
- Wu, X. and H. Liu. (2007a). "Clarification of Aspects in In-line Phase-sensitive X-ray Imaging." *Med. Phys.* 34(2):737–743.
- Wu, X. and H. Liu. (2007b). "Robustness of a Phase-retrieval Approach Based on Phase-attenuation Duality." *J. X-ray Sci. Tech.* 15(2):85–95.
- Wu, X., A. E. Deans, and H. Liu. (2003). "X-ray Diagnostic Techniques," in *Biomedical Photonics Handbook*. Tampa, Florida: CRC Press, 2003.
- Wu, X., G. T. Barnes, and D. M. Tucker. (1991). "Spectral Dependence of Glandular Tissue Dose in Screen-film Mammography." *Radiology* 179:143–148.
- Wu, X., H. Liu, and A. Yan. (2005). "X-ray Phase-attenuation Duality and Phase Retrieval." *Opt. Lett.* 30(4):379–381.
- Wu, X., H. Liu, and A. Yan. (2008). "Phase-contrast X-ray Tomography: Contrast Mechanism and Roles of Phase Retrieval." *Eur. J. Radiol.* 68:S8–S12.
- Yan, A., X. Wu, and H. Liu. (2008). "An Attenuation-partition Based Iterative Phase Retrieval Algorithm for In-line Phase-contrast Imaging." *Opt. Express* 16:13330–13341.
- Yan, A., X. Wu, and H. Liu. (2010). "Performance Analysis of the Attenuation-partition Based Iterative Phase Retrieval Algorithm for In-line Phase-contrast Imaging." *Opt. Express* 18:16074–16089.
- Yan, A., X. Wu, and H. Liu. (2011). "Robustness of Phase Retrieval Methods in X-ray Phase Contrast Imaging: A Comparison." *Med. Phys.* 38(9):5073–5080.
- Zhang, D., H. Liu, and X. Wu. (2008a). "DQE Analysis on a Dual Detector Phase X-ray Imaging System." *Phys. Med. Biol.* 53:5165–5176.
- Zhang, D., J. Rong, R. Chu, X. Z. Wu, and H. Liu. (2006). "Imaging Characteristics of a High Resolution Computed Radiography System." *J. X-ray Sci. Technol.* 14(4):273–282.
- Zhang, D., M. Donovan, L. L. Fajardo, A. Archer, X. Wu, and H. Liu. (2008b). "Preliminary Feasibility Study of an In-line Phase Contrast X-Ray Imaging Prototype." *IEEE Trans. Biomed. Eng.* 55(9):2249–2257.

Advances in Medical Physics

2014

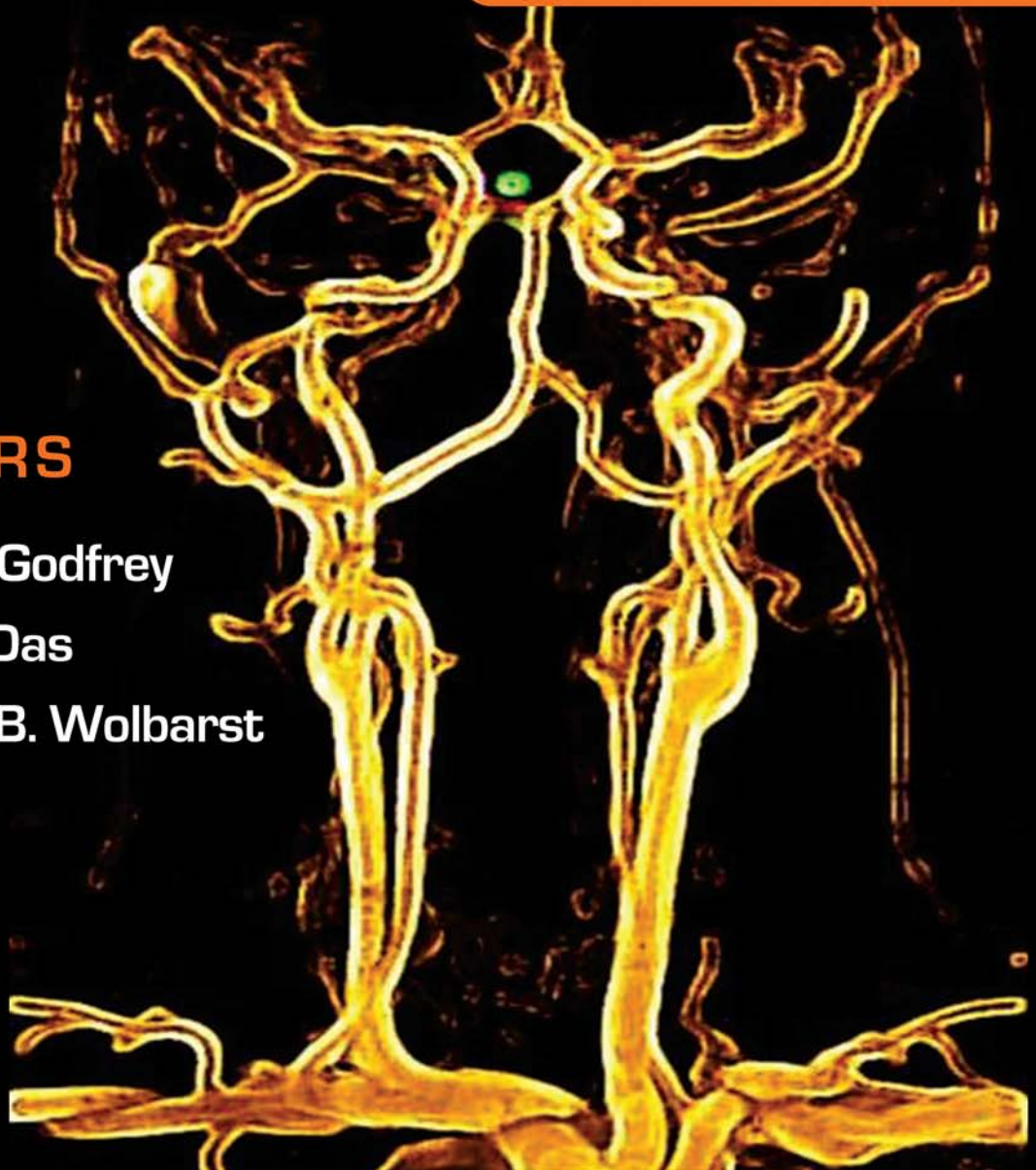
volume 5

EDITORS

Devon J. Godfrey

Shiva K. Das

Anthony B. Wolbarst



M E D I C A L P H Y S I C S P U B L I S H I N G

Contents

Volume 5

Preface	ix
Contributors	xi
Contents of Previous Volumes of <i>Advances in Medical Physics</i>	xiii
2006.....	xiii
2008.....	xiii
2010.....	xiv
2012.....	xv
1 Stereotactic Radiotherapy for Breast Cancer: GammaPod™	1
Elizabeth Nichols, Yildirim D. Mutaf, Steven Feigenberg, and Cedric Yu	
2 Gold Nanoparticles in Radiation Therapy	13
Ross Berbeco	
3 Intra-fraction Motion in Radiation Oncology	21
David H. Thomas and Daniel A. Low	
4 Heavy Ion Therapy	45
Bijan Arjomandy	
5 Methods and Techniques for Comprehensive 3D Dosimetry.....	69
Mark Oldham	
6 Passive Dosimeters for Personnel and Patient Dosimetry.....	87
Steven J. Goetsch	
7 The Role and Impact of the ICRP in Medicine	99
Claire Cousins	
8 The Role of the International Atomic Energy Agency (IAEA) in Global Medical Physics Activities	107
Jacob Van Dyk and Ahmed Meghzifene	
9 Novel X-ray Photonics for Medical X-ray Imaging	123
Susanne M. Lee, Sudeep Mandal, Brian Scherer, and Peter Edic	
10 In-line Phase-sensitive X-ray Imaging	143
Da Zhang, Fanbo Meng, John Rong, Xizeng Wu, and Hong Liu	

11	Parallel Imaging: Moving Beyond the Use of Gradients for Spatial Encoding.....	171
	Nathan E. Yanasak and Anthony B. Wolbarst	
12	MRI Sequences Above and Beyond Spin-echo	199
	Ronald R. Price and Anthony B. Wolbarst	
13	Advances in PET Imaging	217
	Osama Mawlawi and Thomas Beyer	
14	Advances in Cardiac SPECT	235
	Mark Madsen	
15	MRI of the One-dimensional Patient, Part I: A Gentle Approach to Teaching a Challenging Subject to Scientists and Engineers.....	247
	Anthony B. Wolbarst, Kevin F. King, Ron Price, Charles Smith, and Nathan Yanasak	